UCLouvain

FACULTE DES SCIENCES

Faculté des sciences

Study of solar wind expansion: improvement of the Kappa exospheric model and comparison with new observations

Mémoire présenté en vue de l'obtention du grade académique de Master [120] en sciences physiques, finalité approfondie.

Auteur : Charline Audoor
Promotrice : Viviane Pierrard
Lecteurs · rices : Hervé Lamy et Véronique Dehant
École de physique, ELIC
Année académique 2021-2022

Abstract

Lately, two satellites providing very interesting measurements of the Sun have been launched: Parker Solar Probe (12 August 2018) and Solar Orbiter (10 February 2020). Parker Solar Probe travels closer to the surface of the Sun than any other spacecraft before and can provide information that helps to understand the mechanisms that take place in the solar corona.

The solar wind is often studied with a kinetic exospheric model that assumes a certain velocity distribution function for each particle specie of the wind. These models give relatively good results and allow the explanation of various phenomena related to the solar wind by representing the electron distribution by a Kappa distribution associated with an index κ. However, this distribution has limitations and kinetic models cannot compute all the macroscopic quantities for all the values of the κ-index. Recently, Scherer, K., Fichtner, H., and Lazar, M. (2017) introduced the regularized Kappa distribution resolving the critical limits and allowing a fluid description of the solar wind.

The main objective of this work is the improvement of an exospheric model by modifying the electron distribution with the regularized Kappa distribution. In order to be able to analyse the results of the model adequately, this work will be divided into three parts. Since the model assumes a low altitude distribution, the first part will study the shape of the distributions at low distances measured by Parker Solar Probe. The second part will focus on the links that can be observed between solar wind parameters. The final part consists of the comparison of the model with in-situ observations from several satellites.

This work illustrates the relevance of using a regularized Kappa distribution. It also shows the importance of considering suprathermal populations in the models. The exospheric model is a valid model, but by neglecting the Coulomb and wave-particle interactions, it can only reproduce accurately a limited number of moments.

Acknowledgements

I would like to thank all those who have contributed in any way to this paper.

I would first like to thank my family for their support throughout my academic training.

Then I would like to thank my friends, especially Linh Phuong, Simon Jacquet, Pauline Denys and Marie Dockx for their advice and their support during this year.

I would like to thank Jasper Halekas for the distributions of Parker Solar Probe at $17.2R_S$ that allowed me to study velocity distributions at low distances from the Sun.

I would also like to thank Hervé Lamy and Véronique Dehant for accepting to evaluate me.

Finally, I would like to thank my supervisor, Viviane Pierrard, for her advice, her availability, and her kindness. This master thesis was a very nice experience largely thanks to her.

Contents

Acronyms

CMEs Coronal Mass Ejections

HCS heliospheric current sheet

IMF interplanetary magnetic field

MHD magnetohydrodynamics

PSP Parker Solar Probe

RKD regularized Kappa distribution

SolO Solar Orbiter

UY Ulysses

VDF velocity distribution function

Chapter 1

Introduction

1.1 The Sun and its environment

Being the nearest star to Earth, the Sun is an important object of study. The Sun is a hot ball of plasma, a quasi-neutral ionized gas that shows collective behaviour. The very high temperature of the Sun has led to the ionisation of the gas. This state of matter is dominant in the universe and therefore deserves attention.

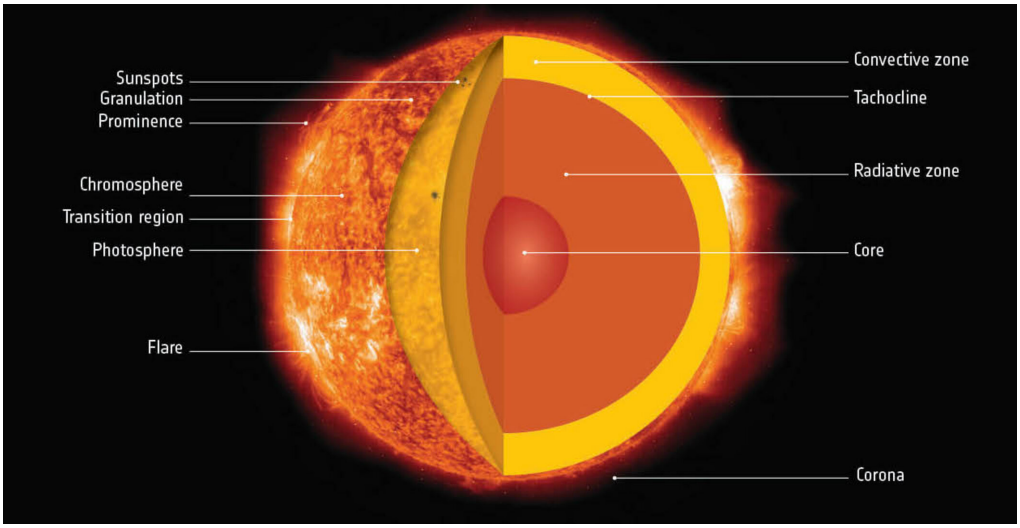

Figure 1.1: The anatomy of the Sun. Source: ESA.

As can be seen in Figure 1.1, the Sun can be decomposed into different layers. The core of the Sun, where nuclear fusion takes place, can reach temperatures up to 10^7 K. The energy is transferred from the centre through the different outer layers. The first layer above the core, the radiative zone, transfers the energy by radiation as its name suggests. The energy is then transferred by convection in the convection zone. Between the two last zones, there exists a transition layer called the tachocline. Within the convection zone, the movement of the plasma creates a huge magnetic field. This magnetic field bursts onto the photosphere, the visible surface of the Sun. These emerging clusters of magnetic fields are called sunspots. These regions are darker due to

the lower temperature and have a higher magnetic field than the surrounding regions in the photosphere.

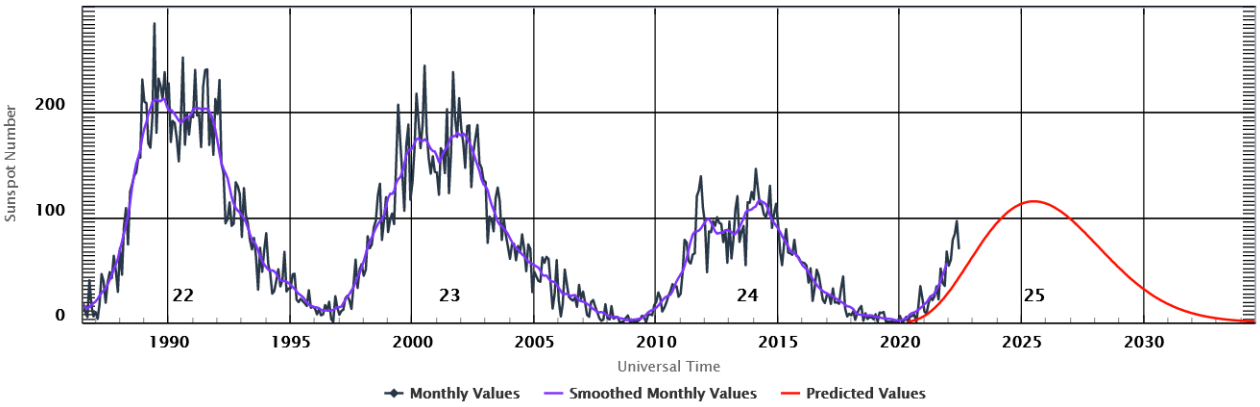

Figure 1.2: Solar cycle progression from 1986 to 2034 from the Space Weather Prediction Center (SWPC).

The Sun's magnetic field is complicated and varies over time. The activity of the Sun, calculated using the number of sunspots, can be expressed in cycles of nearly 11 years. At the end of the 11 years, the magnetic polarity of the Sun flips. On Figure 1.2, it can be seen that the Sun is now at the beginning of the cycle. The last solar minimum occurred end of 2019. The complexity of the magnetic field with the number of small structures at every latitude grows with the activity.

The solar atmosphere, above the photosphere, consists of three layers: the chromosphere, the transition region and the corona. Within the solar atmosphere, the density decreases with distance. Moving away from the main energy source, the temperature should also decrease with distance. Surprisingly, the corona is hotter than the photosphere. The temperature in the transition region increases by two orders of magnitude, separating the chromosphere from the corona. This temperature rise with the distance has also been observed in other stars. This enigma is called the "coronal heating problem". This issue is still being discussed.

In the corona, there are open flux tubes and closed magnetic field loops. When the number of sunspots is minimum, the Sun's magnetic field can be represented in first approximation by a dipole. At large distances from the Sun, the open magnetic field lines of opposite polarity come together and create a thin sheet of electric current, known as the heliospheric current sheet (HCS). With the Sun's rotation, the magnetic field line forms a spiral. This structure is known as the Parker spiral. The tilt between the Sun's axis of rotation and the perpendicular to the plane of the Earth's orbit leads to the undulations of the spiral. This phenomenon is illustrated in figure 1.3.

The regions in the solar corona where the lines of the magnetic fields are open are called coronal holes. Hence, plasma can escape from these regions. These regions are temporary, and their number and size vary with the solar activity. Also, they are relatively cool and

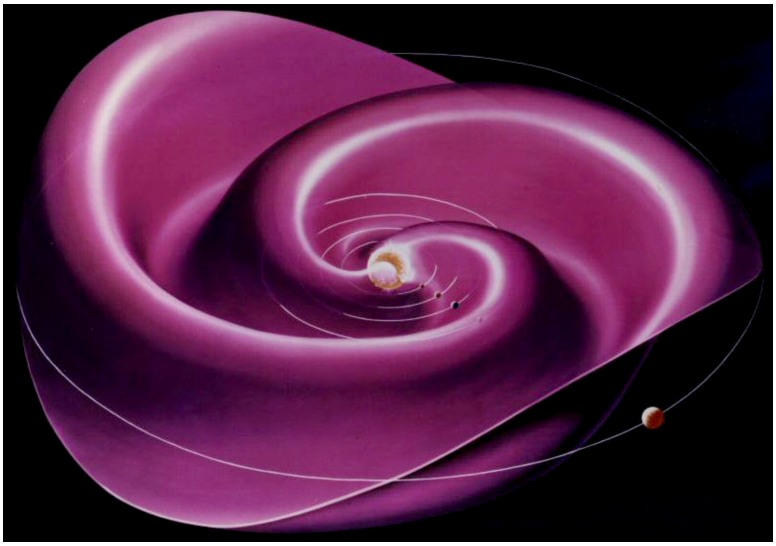

Figure 1.3: Heliospheric current sheet. Source: NASA

less dense than the rest of the solar corona. The escaping plasma flux from the Sun is called solar wind.

1.1.1 Solar wind

More specifically, solar winds are collision-poor plasma. This plasma is made of electrons, protons, alpha particles (about 1% - 5% of the ions) and heavier ions (less than 1%). Because of their difference in mass and charge, the different particle species have different bulk speeds. These charged particles are affected by the gravitational force as well as the electric and magnetic fields. Solar winds can conduct electric currents and carry the interplanetary magnetic field (IMF).

One differentiates two solar wind types: slow (250-450 km/s) and fast (450-800 km/s) solar winds. This distinction allows different characteristics to be highlighted, such as the difference in origin. Indeed, during its first two orbits, the spacecraft Ulysses observed that the velocity varies with the latitude and with solar activity. As can be seen in Figure 1.4, during low solar activity, slow solar winds come from streamers near the equatorial plane with a higher density and fast solar winds from the high latitude with a lower density. During high solar activity, fast and slow solar winds originate from all latitudes.

When one observes the solar corona, one can see that during low solar activity, coronal holes appear close to polar regions with bright complex structures between mid-latitudes. During maximum solar activity, coronal holes appear at all latitudes and in smaller sizes with bright structures all around the star. With these structures, it is easy to deduce that fast winds should originate from the relatively calm regions that are the coronal holes.

When a fast solar wind catches up with a slow solar wind, it creates a shock front. This collision zone can only be observed near the HCS. This collision compresses the slow solar

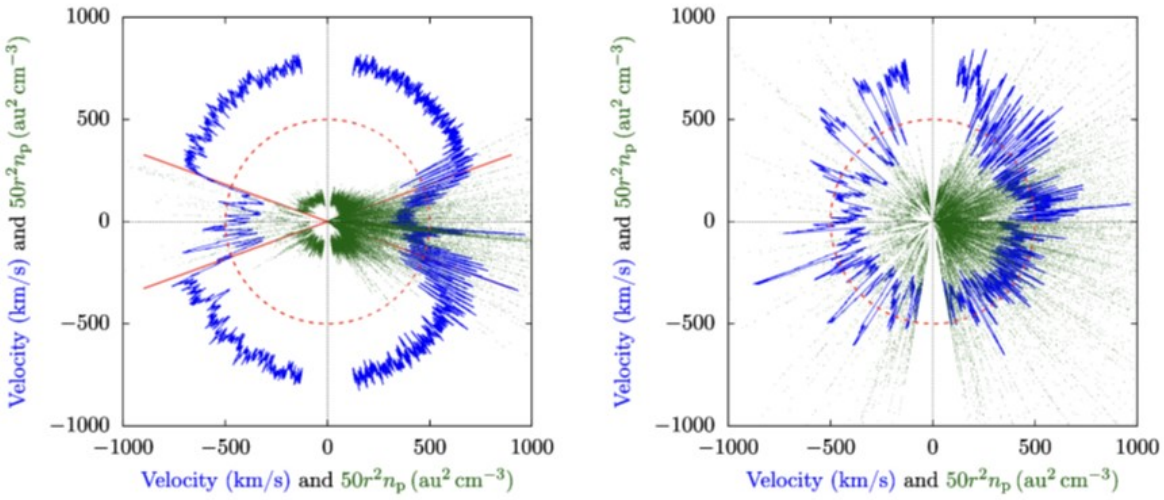

Figure 1.4: Polar plots of the proton radial velocity (blue) and density (green) of the solar wind at different heliographic latitudes. The left plot represents data near the solar mimimum for cycle 22 and the right plot near the solar maximum for cycle 23 observed by Ulysses. Source: Verscharen, D., Klein, K. G., and Maruca, B. A. (2019).

wind and accelerates the latter.

1.1.2 Space weather

The Sun continually releases this flow of energetic charged particles that fill the interplanetary space. The solar wind and the IMF, together determine the environment around the Earth and the other planets of the solar system. The wind is influenced by energetic events produced by the Sun. These are related to the relatively new discipline of space weather, studying the conditions in the space environment.

Energetic particles of solar winds can be harmful to astronauts and technologies. Around the Earth, solar winds can trigger geomagnetic storms, a disturbance of the Earth's magnetosphere. Thereby, they can cause satellites orbiting the Earth to break down, disturb radio transmissions and there may be repercussions on the electrical network. While penetrating the earth atmosphere, solar winds can also cause less damaging phenomena like auroras.

Space weather events are more likely to occur during a maximum of solar activity due to the higher frequency of phenomena such as spontaneous expulsions of coronal plasmas, called Coronal Mass Ejections (CMEs).

1.2 Kinetic approach

There are two main approaches to studying plasma: the kinetic and hydrodynamic approaches. The kinetic approach is complex but describes the physics in detail by allowing a microscopic description of the gas or plasma using the velocity distribution

function (VDF) of the different types of particle. When the plasma is very hot and very rare, it is particularly useful to take a kinetic approach.

In the chosen approach, the particles are described with a position and a velocity at time t in the phase space, the set of all possible positions $\mathbf{r}$ and velocities $\mathbf{v}$. Thus, the distribution function f_j, for a particle species j, represents the number of particles j in a volume $d^3\mathbf{r}d^3\mathbf{v}$ centred in $\mathbf{r}$ and $\mathbf{v}$ at a time t of the phase space. The number of particles N_j can be calculated with

$$dN_j = f_j(\mathbf{r}, \mathbf{v}, t)d^3\mathbf{r}d^3\mathbf{v} \tag{1.1}$$

With the distribution function, one can calculate macroscopic quantities with moments of specific orders, the power of the velocity. Moments of an order l of the distribution function have a form as followed:

$$M_j^{(l)} \sim \int_{-\infty}^{\infty} (\mathbf{v} - \mathbf{u}_j)^{(l)} f_j(\mathbf{r}, \mathbf{v}, t)d^3\mathbf{v} \tag{1.2}$$

The calculation of the moments allows the determination of quantities such as the number density (moment of order 0):

$$n_j(\mathbf{r}, t) = \int_{-\infty}^{\infty} f_j(\mathbf{r}, \mathbf{v}, t)d^3\mathbf{v} \tag{1.3}$$

the bulk velocity (moment of order 1):

$$\mathbf{u}_j(\mathbf{r}, t) = \frac{\mathbf{F}_j(\mathbf{r}, t)}{n_j} = \frac{1}{n_j} \int \mathbf{v} f_j(\mathbf{r}, \mathbf{v}, t)d^3\mathbf{v} \tag{1.4}$$

where $\mathbf{F}_j(\mathbf{r}, t)$ is the particle flux, the pressure tensor (moments of order 2):

$$\mathbf{P}_j(\mathbf{r}, t) = m_j \int f_j(\mathbf{r}, \mathbf{v}, t)(\mathbf{v} - \mathbf{u}_j)(\mathbf{v} - \mathbf{u}_j)d^3\mathbf{v} \tag{1.5}$$

the mean temperature:

$$T_j(\mathbf{r}, t) = \int \frac{m_j}{3n_j k_B} |\mathbf{v} - \mathbf{u}_j|^2 f_j(\mathbf{r}, \mathbf{v}, t)d^3\mathbf{v} \tag{1.6}$$

the heat flux tensor (moments of order 3):

$$\mathbf{Q}_j(\mathbf{r}, t) = \frac{m_j}{2} \int (\mathbf{v} - \mathbf{u}_j)(\mathbf{v} - \mathbf{u}_j)(\mathbf{v} - \mathbf{u}_j) f_j(\mathbf{r}, \mathbf{v}, t)d^3\mathbf{v} \tag{1.7}$$

where k_B is the Boltzmann constant and m_j is the mass of the particle specie j.

1.3 Observed proton and electron VDF

One can now clearly understand why it is important to know the VDF. When plasmas are in thermodynamic equilibrium with no external forces, the VDF has a Maxwellian distribution. Coulomb collisions preserve the local thermodynamic equilibrium. This distribution is often that of gases. The Maxwellian distribution can be expressed as:

$$f_M(v_\parallel, v_\perp) = \frac{n}{\pi^{3/2}\theta_\perp^2\theta_\parallel} \exp\left(-\frac{v_\parallel^2}{\theta_\parallel^2} - \frac{v_\perp^2}{\theta_\perp^2}\right) \tag{1.8}$$

where $v_\parallel$ and $v_\perp$ are the parallel and perpendicular velocities to the magnetic field and

$$\theta_{M,\perp} = \sqrt{\frac{2k_B T_{M,\perp}}{m}} \tag{1.9}$$

$$\theta_{M,\parallel} = \sqrt{\frac{2k_B T_{M,\parallel}}{m}} \tag{1.10}$$

are the characteristic thermal speeds.

Nevertheless, suprathermal tails are generally observed in space plasmas like the solar wind, the magnetosphere of the Earth and other planets. These observations seem to indicate a universal mechanism for their creation (Pierrard, V. and Lazar, M. (2010)).

This non-Maxwellian population, that decreases as a power law, is generally well represented by the Kappa distribution described by a parameter κ (Binsack (1966)Vasyliunas (1968)). Different expressions are used in the literature to refer to the Kappa distribution. One can rather talk about a family of Kappa distribution functions. The original Kappa distribution, also known as the Olbertian distribution, is defined as:

$$f_K(v_\parallel, v_\perp) = \frac{n}{(\pi\kappa)^{3/2}\theta_\perp^2\theta_\parallel} \frac{\Gamma[\kappa+1]}{\Gamma[\kappa-1/2]} \left(1 + \frac{v_\parallel^2}{\kappa\theta_\parallel^2} + \frac{v_\perp^2}{\kappa\theta_\perp^2}\right)^{-\kappa-1} \tag{1.11}$$

where $\Gamma[x]$ is the Gamma function and $\theta_\perp$ and $\theta_\parallel$ are the thermal velocity that are associated with the Maxwellian one and is independent of the Kappa parameter. With the Olbertian, it is the temperatures $T_{\kappa,\perp}$ and $T_{\kappa,\parallel}$ that are influenced by the parameter κ.

Figure 1.5 shows the Olbertian Kappa distribution for different values of the index κ. One can see that when the kappa parameter tends to infinity, $\kappa \to \infty$, this Kappa distribution returns to the Maxwellian distribution. This index represents the slope of the energy spectrum of the suprathermal population.

As explained in the previous section, the VDF will be used to calculate the moments with equations 1.3-1.7. However, with a Kappa distribution, to ensure convergence of a moments of order l, the kappa index κ must have a value that satisfies $\kappa > (l+1)/2$. Thus, to define the temperature, the κ parameter must be $\kappa > 3/2$.

As described above, solar winds are mainly composed of protons and electrons. The electron VDF (eVDF) used to be fitted by two Maxwellians but Maksimovic, M., Pierrard, V., and Riley, P. (1997) showed that a single Olbertian Kappa distribution was more accurate. The use of this distribution allows to reveal the global anti-correlation between the bulk speed and the kappa parameter. Fast solar winds have higher suprathermal tails

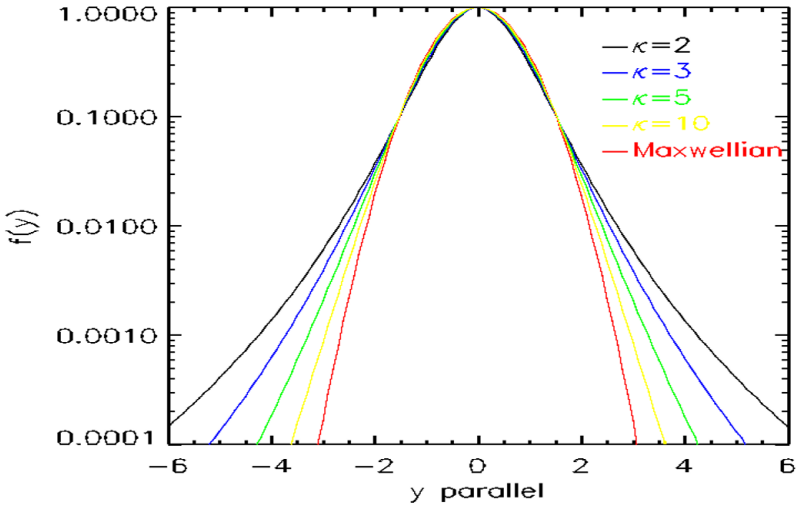

Figure 1.5: The Kappa distribution for different values of the parameter kappa κ from Pierrard, V. and Lazar, M. (2010).

and slow solar winds are closer to a Maxwellian. This is not surprising since the collision cross section decreases with a higher velocity. Thus, fast solar winds must have VDFs that move further away from the Maxwellian VDF.

A standard fit of the eVDF consists of a thermal core (a few 10 eV), a suprathermal halo (about 70-2000 eV) and a strahl (similar energy range as the halo). The dominant core (about 90% of the number density) is described by a standard Maxwellian while the halo and the strahl are, as discussed before, well described by a Kappa distribution (Pierrard, V. and Lazar, M. (2010)) because the tails decrease as power laws and not exponentially. The halo is quasi-isotropic while the strahl is generally only in the parallel and antisunward direction to the magnetic field. As can be seen in the top pannel of Figure 1.6, the population in the direction parallel to the IMF (black line) is enhanced due to the strahl. In the figure, the core is well fitted by the Maxwellian distribution (in red).

Another power law, known as the super halo, can also be present at higher energies (above 2keV) (Lin (1998)). The number density of this population is low and the population is mostly isotropic (Yang et al. (2015)).

Regarding the protons, their VDF is characterized by beams aligned to the IMF and high temperature anisotropy (a difference in the parallel and perpendicular temperature to the IMF) (Marsch et al. (1982)).

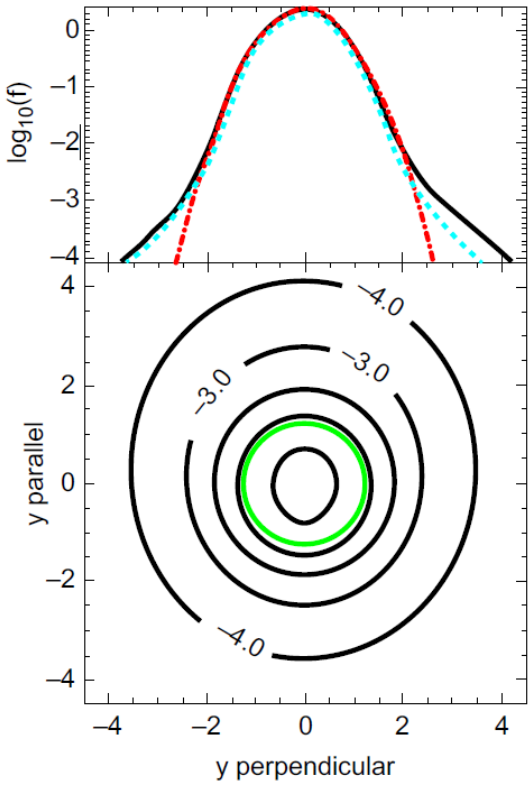

Figure 1.6: A standard eVDF observed at 1 AU by the spacecraft Wind. Top pannel : The cross section of the parallel (black) and perpendicular (blue) eVDF to the IMF. A Maxwellian (red) fits the core. Bottom panel : the isocontours of the distribution as a function of the parallel and perpendicular velocity. Source: Pierrard (2012b).

Suprathermal population

The suprathermal tails become more important by moving away from the Sun. This suprathermalisation with the radial distance is manifested by the decrease in the kappa value. This decrease is observed for both the halo and the strahl (Štverák et al. (2009)). Štverák et al. (2009) showed that both kappa parameters continuously decrease and beyond 1 AU stay relatively constant. By observing that the relative density of the halo and the strahl vary in opposite ways, while that of the core stays almost constant, one can assume that the suprathermalization is due to a diffusion of the strahl electrons into the halo with distance (Maksimovic et al. (2005), Štverák et al. (2009)).

The suprathermalization is less present for slow solar winds. Above 1AU, Ulysses shows a value of the kappa index between 2 and 7 for the fast solar wind by fitting the observed VDF with a single (Olbertian) kappa distribution (Maksimovic, M., Pierrard, V., and Lemaire, J.F. (1997)). However, between 1.5 and 2.3 AU, this index stays roughly constant (Le Chat et al. (2011)).

1.4 The exospheric model

The exospheric approach is applicable at a certain altitude above the Sun, where the collisions are negligible (Jockers (1970)Lemaire, J. and Scherer, M. (1971)). Thereby, one will introduce the exobase: the transition region between the collision-dominant and collision-negligible regime. To determine the collision regime, one uses the Knudsen number Kn, the ratio of the particle mean free path λ to the density scale height H. The

exobase is then defined as the region where the Knudsen number is equal to one. These quantities can be expressed as:

$$Kn = \frac{\lambda}{H} \qquad \lambda = \frac{1}{n\sigma} \qquad H = -\left(\frac{d\ln n}{dr}\right)^{-1} \tag{1.12}$$

where n is the number density and σ is the collision cross section of the particle.

Three regions above the Sun can be distinguished: the barosphere, the exobase and the exosphere. Under the exobase, in the barosphere, the collisions are dominant ($Kn < 1$). In this region an hydrodynamic approach is more appropriate. Above the exobase, in the exosphere ($Kn > 1$), the collisions are negligible and only long-distance interactions are considered. The time evolution of the distribution function can in this regime be described with the Vlasov equation for plasma. At the exobase, the time evolution is described by the Fokker-Planck equation.

Some models to study solar wind have been developed using the kinetic approach. When these models consider that there is no collision above the Sun, they are referred to as exospheric models. In this case, only external forces are considered. VDFs are assumed at the exobase and are affected by the gravity, electric and magnetic field along its radial evolution. By neglecting wave-particle interactions, the kinetic model is very simplified. However, a kinetic model can be used to understand some of the physical processes, like solar wind acceleration or the high temperature in the corona.

Due to the absence of collision and due to the magnetic field, the VDF of the particles can be determined through the conservation of the total energy

$$E = \frac{mv^2}{2} + m\phi_g + ZeV(r) = cst$$

and through the adiabatic invariant of magnetic moment

$$M = \frac{mv^2 \sin^2\alpha}{2B} = cst$$

where m is the mass of the particle, v the velocity, ϕ_g is the gravitational potential, Ze is the charge, $V(r)$ the interplanetary electrostatic potential, α the pitch angle and B the magnetic field (Pierrard, V. and Lemaire, J. (1996)). The pitch angle α is the angle between the magnetic field and the velocity. Any VDF that satisfies these relations is a solution of the Boltzmann and Vlasov equations.

As shown in Figure 1.7, in an attractive potential, there are 4 types of orbits above the exobase depending on the velocity and the pitch angle of the particle. In a repulsive potential there are only escaping and incoming orbits. The particles travel along the magnetic field lines. The escaping particles correspond to the particles with a speed higher than the escaping velocity. The ballistic particles fall back towards the Sun since their kinetic energies are not high enough. The trapped particles are caught between two reflection points. The incoming particles are coming from the interplanetary space.

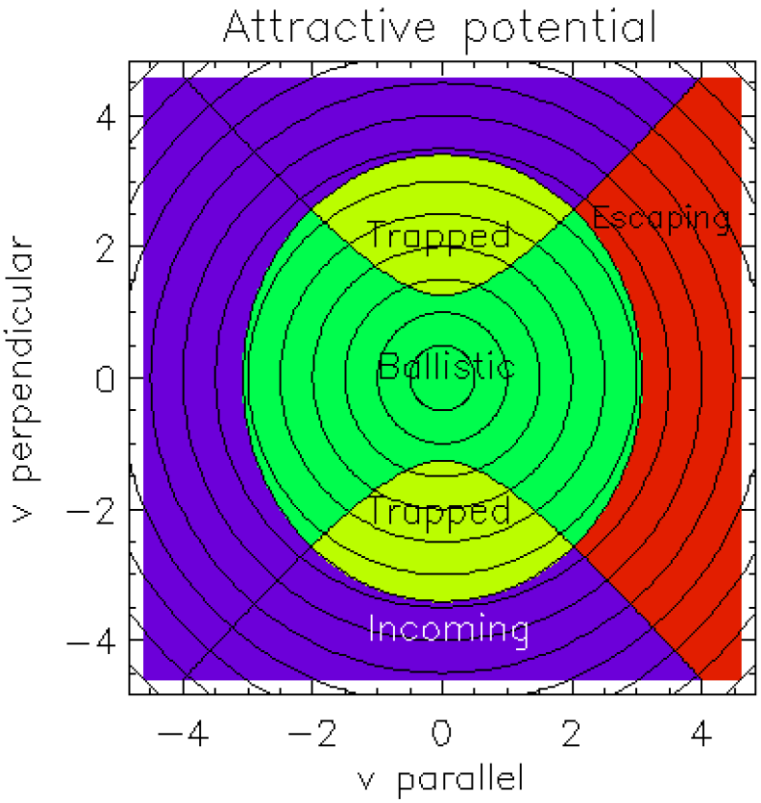

Figure 1.7: The isocontours of the VDF of a particle in an attractive potential. The different colors represent the different orbits of the particle. Source: Pierrard (2012a)

As explained, in order to escape, particles must have velocities higher than the escaping velocity:

$$v > \sqrt{2\phi_g + \frac{2ZeV(r)}{m}}$$

Thus, electrons, that have a lower mass than the ions, escape the gravitational potential more easily. The electrons and ions, held apart in the gravitational field, produce the electrostatic potential $V(r)$. The electrostatic potential induces a polarisation electric field that keeps the plasma quasi-neutral. To calculate the polarisation electric field in an ion exosphere, the model must consider the quasi neutrality ($n_e(r) = n_p(r)$) and the zero net currents ($F_e(r) = F_p(r)$) at each distance.

1.4.1 Solar wind acceleration

The total potential is the sum of the electrostatic and the gravitation potentials. When the particles are in an attractive potential, only the energetic particles can escape. Thus, in the electron VDF, only the suprathermal particles contribute to the flux and heat flux. Kappa distributions for the electrons have thus a higher flux than the Maxwellian. When the kappa parameter decreases, the suprathermal tails of the electrons are higher. To keep the quasi-neutrality, the electrostatic potential increases to result in a higher proton flux. This leads to a higher solar wind speed. By using Maxwellian VDF in the model, one obtains too low solar wind bulk velocity. The Kappa VDF must be

considered to have realistic bulk speeds (Pierrard, V. and Lemaire, J. (1996)).

Suprathermal protons do not have a significant impact compared to the other protons in the distribution on the bulk speed since protons are mainly in a repulsive potential and all protons can escape whatever their speed. The Maxwellian and Kappa distributions can then be used as they are both solutions of the Vlasov equation. However, the proton total potential energy is not a monotonically decreasing function. Below a certain distance r, the proton gravitational potential is greater than the electrostatic potential. Thus, at low altitudes, when the proton total potential is not yet repulsive, protons can have ballistic trajectories. At very low distances from the Sun, only the energetic protons escape.

Due to the lower density of coronal holes, the altitude of the exobase is lower in the regions where the fast solar winds originate. When one considers a lower exobase in the kinetic model, the solar wind reaches higher speeds (Lamy et al. (2003)). At low altitude, when the proton total potential is attractive, the polarization electric field increases explaining the high velocity of solar winds coming from coronal holes. Also, the smaller κ value in coronal holes involves larger tails. As explained above, the energetic population leads also to an increase in speed.

1.4.2 Consequences of suprathermal particles on the heat flux

As explained above, the heat flux is mainly due to the electrons and more particularly their suprathermal population. The Coulomb collision cross section depends strongly on the velocity. Therefore, the particle mean free path of suprathermal particles is greater than the thermal one (Shoub (1983)). In collision dominated regimes, suprathermal tails are then less affected by the Coulomb collision. This may affect the calculation of the heat flux.

Indeed, in the classical theory, the heat flux could be approximated by the classical collisional Spitzer–Härm expression as is the case with the Maxwellian distribution. Landi, S. and Pantellini, F.G.E. (2001) showed that in the corona for low values of kappa, the heat flux moves away from the Spitzer–Härm value and takes on a sign opposite to it. Landi, S., Matteini, L., and Pantellini, F. (2014) show that the heat flux of solar winds, for Kn larger than 0.01, does not approach the classical collisional Spitzer–Härm limit. The VDF contains in this collision regime ($Kn > 0.01$) suprathermal tails.

This demonstrates that the suprathermal tails must be well considered in space plasmas. This also reveals the unsuitability of the classical heat conduction law.

1.4.3 Coronal heating

The velocity filtration effect, proposed by Scudder (Scudder (1992b),Scudder (1992a)), explains the high temperature in the corona. This non dissipative mechanism is based on the filtration of the particles by the solar gravitational/electrostatic potential. In an attractive potential, the ratio of suprathermal on thermal particles grows with

the altitude. Therefore, with a non-Maxwellian distribution in the transition region, the temperature should increase with altitude. This mechanism explains the positive temperature gradient without the need for an additional heating energy source.

This effect induces an anticorrelation between the temperature and the density. Pierrard, V. and Lamy, H. (2003) use this mechanism to explain the higher than expected temperatures of heavy ions in fast solar winds. Using isotropic Kappa distributions in the solar corona, they show that the temperature naturally increases, not only for electrons and protons, but also for the other ions more than proportionally to their mass.

Many other mechanisms have been developed to explain the temperature of the corona. These other mechanisms are referred to as dissipative: magnetic energy is transformed into heat by a dissipative process. Two main processes are generally discussed:

- heating through small reconnection events
- heating by the energy in the production of waves

Chapter 2

Fit of velocity distribution function observed at low altitude

2.1 Introduction

In this chapter, we will focus on the VDF of ions and electrons observed near the Sun. This analysis consists of one distribution of protons and one of electrons. To deduce specific characteristics of the VDF, a statistical analysis of a large number of events is required. However, these typical distributions can already provide information about the overall shape of the distribution. At low altitudes, the solar wind is more primitive and is closer to the VDF from the outer corona of the Sun. As explained, this allows a better understanding of some of the phenomena such as solar wind acceleration and heating.

Maksimovic, M., Pierrard, V., and Lemaire, J.F. (1997) have fitted observed electrons VDFs of Ulysses at large radial distance with a single Olbertian Kappa. More precise VDF analysis showed more three populations: core, halo, and strahl. Exospheric models such as those in Lemaire, J. and Scherer, M. (1971), Maksimovic, M., Pierrard, V., and Riley, P. (1997) and Lamy et al. (2003), consider a single Olbertian distribution for the eVDF at the exobase. One may wonder to what extent this distribution remains valid at low altitudes.

These close measurements from Parker Solar Probe are especially interesting because of their novelty. Indeed, it is the first time a space mission can measure the distribution so close to the Sun, below the orbit of Mercury.

2.1.1 Parker Solar Probe

On 12 August 2018, the mission Parker Solar Probe (PSP) has been launched by NASA. The special feature of PSP is that it travels through the Sun's atmosphere at distances that no other satellite has reached before. The proximity to the Sun with its extreme temperatures makes this mission particularly difficult.

PSP completed its 12th perihelion on the 1st of June 2022. It travels below the orbit of Mercury and will reach distances below $10R_S$ in 2024. PSP is a real exploration mission.

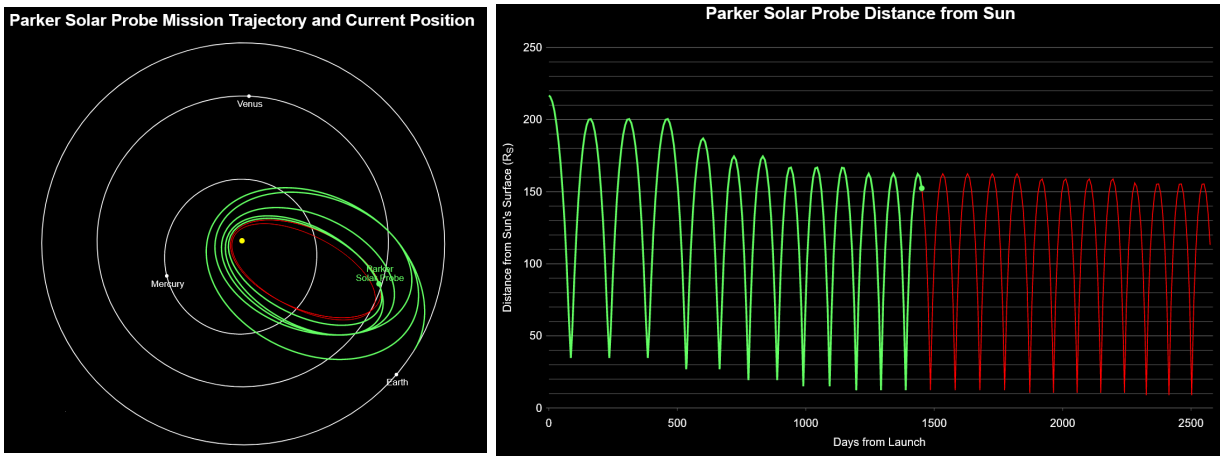

Figure 2.1: The orbit of Parker Solar Probe from the launch until 3 August 2022 (in green) from The Johns Hopkins University Applied Physics Laboratory.

These new observations will allow interesting studies on the extension of the solar corona. The aim of this mission is to study the solar corona and the solar wind, to, among other issues, help to understand the origin and the acceleration of solar wind.

On 10 February 2020, ESA with the participation of NASA launched Solar Orbiter (SolO). SolO orbits the Sun at distances reaching 0.22 AU (or about 60 R_S), roughly at Mercury's perihelion, and will reach an inclination of 24° to the solar equator. At this distance, the wind is still in a primitive state. Its main objective is to understand how the sun impacts its environment through high-resolution close-up data. The study of solar winds is therefore also among its objectives. This probe is less useful for this analysis since it does not go to such low distances. However, SolO with PSP makes the current period attractive for solar physicists.

2.2 Data

The data that will be studied here were taken at a distance of 17.2 R_S. PSP measured in-situ the flux $\log_{10} f$ and the pitch angle as a function of the energy (eV) for the ions and the electrons of the solar wind. As a reminder, the pitch angle is the angle that the velocity vector of the charged particle forms with the local magnetic field. These data were provided by Jasper Halekas from University of Iowa and were measured with the Solar Probe ANalyzers (SPAN) sensor. The SPAN instruments (SPAN-E for electrons and SPAN-Ion for the ions) are electrostatic analyzers that take part in the Solar Wind Electrons Alphas and Protons (SWEAP) Investigation. A description of the investigation can be found in Kasper et al. (2016) and specifically for SPAN-E in Whittlesey et al. (2020).

The electrons and protons distributions obtained are shown in Figure 2.2. They are presented as a function of the perpendicular velocity and the parallel velocity to the IMF.

The measured energies for the ions are between 11.67 and 1629.53 eV and for the electrons

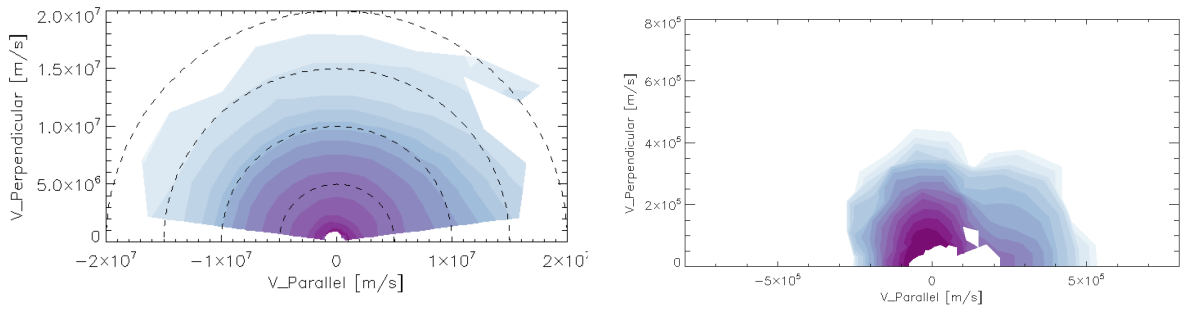

(a) Electrons

(b) Ions

Figure 2.2: Electron and proton distributions at small distance (17,2 R_S) observed by PSP as a function of $v_{\parallel}$ and $v_{\perp}$ with respect to the IMF.

between 0.88 and 1830.42 eV. Since the energies of the particles remain below $mc^2/100$, no relativistic transformation is needed between the energy and the velocity.

2.3 Fitting Process

To derive some of the bulk parameters, the fitting technique is often used in plasma physics. Given the distribution obtained, 1D fits will be performed here in different directions.

The ions in the solar wind consist mainly of protons. The proton VDF generally consists of a core with beams and drifts. In each direction, the isotropic form of the Maxwellian from equation 1.8 will be used for the core. The latter is expressed as:

$$f_M(v) = \frac{n}{\pi^{3/2}\theta^{3/2}} \exp\left(-\frac{v^2}{\theta^2}\right) \tag{2.1}$$

where v is the particle velocity and $\theta = \sqrt{2k_BT/m}$ is the associated thermal speed.

As for the electrons, their VDF can be expressed as:

$$f = f_c + f_h + f_s$$

where f_c, f_h and f_s correspond respectively to the VDF of the core, halo and strahl. In view of the profile obtained, one will add a distribution f_{super} for the superhalo population. The fit of the thermal core is also done with a Maxwellian distribution from equation 2.1. For the suprathermal population, i.e. f_h, f_s and f_{super}, a fit with a Kappa distribution is more convenient because the tails decrease as a power law and not exponentially.

The Olbertian distribution is characterised by a temperature T_κ that depends on the index κ in contrast to its kappa-independent thermal speed θ. By changing to a distribution called the modified kappa distribution, the temperature T_κ no longer depends on the

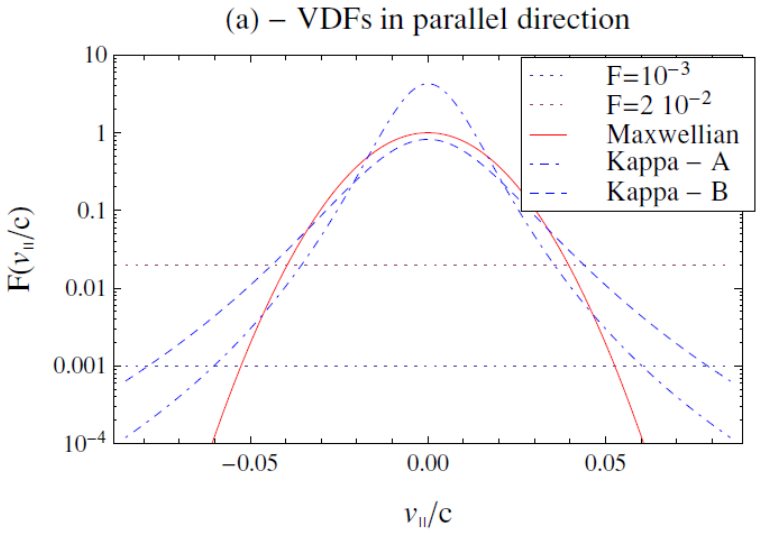

Figure 2.3: A comparison of the Olbertian Kappa distribution (Kappa - B), the modified Kappa distribution (Kappa - A) and the associated Maxwellian distribution. Source: Lazar, M., Fichtner, H., and Yoon, P.H. (2016)

index κ and the now κ-dependent thermal speed has no longer any special meaning. The modified isotropic kappa distribution is defined as:

$$f_\kappa(v) = \left(\frac{m}{2k_B\pi(\kappa-3/2)}\right)^{3/2} \frac{n}{T^{3/2}} \frac{\Gamma[\kappa+1]}{\Gamma[\kappa-1/2]} \left[1+\frac{m}{2k_B(\kappa-3/2)}\left(\frac{v^2}{T}\right)\right]^{-\kappa-1} \tag{2.2}$$

As can be seen in Figure 2.3, this change implies that the modified Kappa and the Maxwellian have the same temperatures, while the Olbertian has a higher temperature but a core similar to the Maxwellian with higher tails. Thus, to highlight the suprathermal population, it is more relevant to study the halo with an Olbertian distribution (Lazar, M., Fichtner, H., and Yoon, P.H. (2016)). Its temperature being different from the Maxwellian one, comparison studies are more interesting. However, the modified Kappa distribution is useful from a computational point of view. The latter distribution will be used to follow the same approach as for the main part of the current literature. The physical system being addressed is also relevant to the choice of distribution (Lazar, M., Fichtner, H., and Yoon, P.H. (2016)).

We will still proceed to a global fit with an Olbertian distribution to see the effects of suprathermal tails and to make the comparison with the exospheric models. It will be performed on the whole distribution and not restricted to the suprathermal population. This fit is interesting given that the exospheric model used in Chapter 4 (Pierrard, V. and Lemaire, J. (1996)) considers a single Olbertian Kappa distribution for the eVDF at the exobase.

The Maxwellian fit on the observations will estimate n and T for each species, while the modified Kappa and the Olbertian Kappa fit will estimate n, T and the power-index κ.

In order to distinguish clearly the halo and strahl populations, the parallel and perpendicular distributions to the IMF will mainly be analysed. With the diffusion of the strahl particles in the halo, one should expect to have a larger strahl population in a narrower pitch angle width (PAW) at lower altitudes (Štverák et al. (2009)). Strahls are generally found in fast solar winds (Rosenbauer et al. (1977)). Anderson et al. (2012) showed that very narrow strahl were usually accompanied by counterstreaming strahls and usually associated with CME (Gosling et al. (1987)). This counter-strahl is much rarer than the strahl. In these situations, particle scattering by wave-particle interactions is less able to overcome the magnetic focus of the strahl (Anderson et al. (2012)).

In order to ensure to observe the strahl population, one looks at pitch angles close to 0°. Given the data obtained, the distributions at a pitch angle of 82.5° and 97.5° are associated with the suprathermal populations of the halo, at a pitch angle of 7.5° of the strahl (with the isotropic population of the halo) and at a pitch angle 172.5° with the counter-strahl (and the halo). Due to the lack of low positive parallel velocity data for protons, an additional fit was made at a pitch angle of about 22.5°.

To differentiate the thermal from the suprathermal population, a breakpoint energy is defined. In this fit, the breakpoint energy was defined between 2.5 10^3 and 3 10^3 km/s, which is equivalent to 17.8 and 25.6 eV. In view of the second power law observed, the suprathermal electron fit was subsequently restricted to a maximum velocity of 13000 km/s, or in energy terms 480.4 eV.

2.4 Results

2.4.1 Electrons

Figure 2.4 represents fits for the distribution near the pitch angle of 90°. At this direction, the suprathermal should mainly consist of the halo. The black dots represent the observations by PSP, the blue line corresponds to the Maxwellian fit, the orange line to the fit with a Kappa distribution and the black line, represents the sum of the distributions $\log f$. The fit was obtained by the nonlinear least squares method. The R^2 values in the tables correspond to the coefficient of determination expressed as follows:

$$R^2 = 1 - \frac{SS_{res}}{SS_{tot}} \tag{2.3}$$

where SS_{res} is the residual sum of squares and SS_{tot} is the total sum of squares. In the best case, where the fitted values would be equivalent to the observations, this coefficient would have a value of 1. Table 2.1 gives the values of these coefficients for three different fits that we will discuss.

Figures 2.4a and 2.4b respectively show the Maxwellian + Kappa fit and the single Olbertian fit. At high speeds, a second power law is observed. To take the superhalo population into account, the energy range for the fit was restricted, as shown in figure 2.4c.

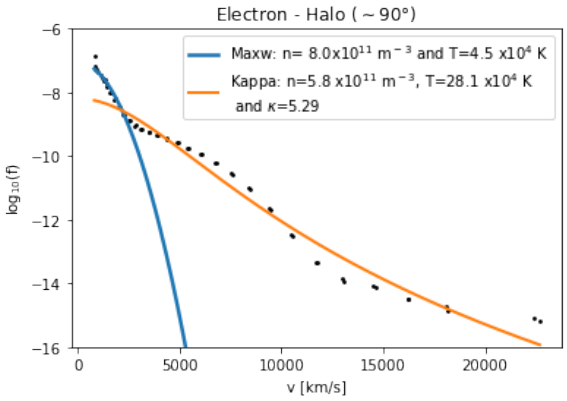

(a) Maxwellian and Kappa fit (R^2 of 0.94)

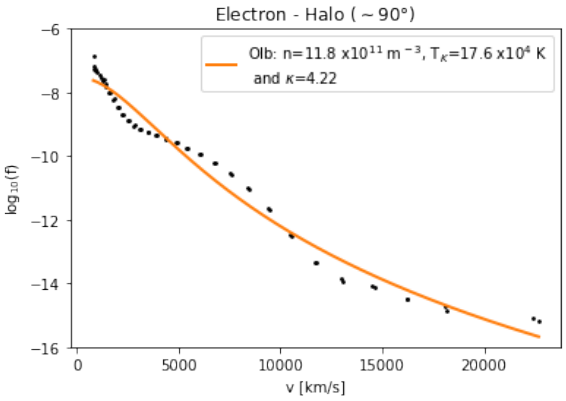

(b) Olbertian Kappa fit (R^2 of 0.98)

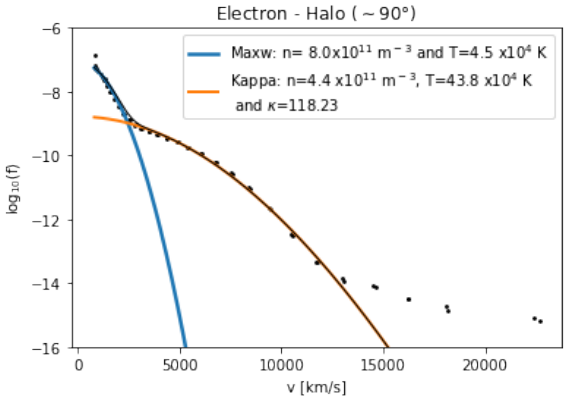

(c) Maxwellian and Kappa fit on the velocities under 13000 km/s (R^2=0.48 for the whole distribution and R^2=0.99 for $v < 13000$ km/s)

Figure 2.4: Electron velocity distribution measured by PSP at a distance of 17.2 R_S and at a pitch angle of 82.5° and 97.5°. The observations are indicated by the black dots. The blue line is the Maxwellian fit and the orange line is the Kappa fit. The black line is the sum of the different distributions in a fit.

R^2	7.5°	22.5°	82.5°-97.5°	172.5°
Maxw+Kap	0.997	0.997	0.982	0.978
Maxw+Kap (<1300km/s)	0.995	0.997	0.994	0.991
Olbertian	0.960	0.969	0.974	0.978

Table 2.1: The coefficient of determination R^2 for the pitch angle 7.5°, 22.5°, 82.5°-97.5° and 172.5°. These are obtained from the fit of a Maxwellian (Maxw) and a modified Kappa (Kap) distribution on all the electron velocity, the same fit but only adjusted to suprathermal speeds below <1300km/s and the fit from a single Olbertian Kappa distribution.

The single Olbertian distribution fits relatively well the whole distribution, as can be seen with the R^2 coefficient in Table 2.1. Its suprathermal tails can represent the distribution at high energies. However, as can be clearly seen in the figure 2.4c, to

represent each population correctly, several distributions must be used. The sum of the Maxwellian and modified Kappa distribution, adjusted to the correct energy ranges, characterises the different populations more precisely. Note that the high value of the kappa index obtained on Fig. 2.4c indicates that a fit with a second Maxwellian would also give an excellent fit on this energy range.

To that end, adding an adjustment for the super halo population would make the distribution much more valuable. By fitting this population with the same modified Kappa distribution as before, the latter increased the thermal population considerably. Figure 2.5 represents in red the modified Kappa fit for the superhalo. When analysing this function up to negative speeds, the fit does not give a realistic VDF. Also, the high density parameters n obtained are inconsistent. The same issue arises when using an Olbertian distribution. Given the limited data at high speed, a fit for the superhalo is less accurate. This one is also probably better represented with another distribution.

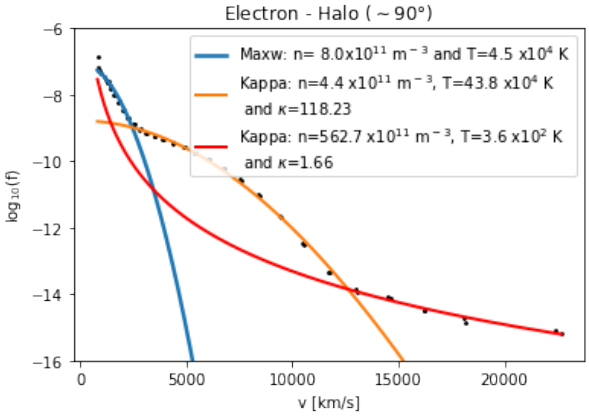

Figure 2.5: A Maxwellian fit for the core, and two modified Kappa fits for the populations at higher energies: halo and superhalo. The black dots are the measured distribution of PSP at a pitch angle of 82.5° and 97.5° (halo). The blue line is the Maxwellian fit and the orange and red line are the modified Kappa fits of the electron distribution.

Figures 2.6a and 2.6b show the two different fits in the direction of the strahl. The κ index obtained for the Olbertian fit is close to 2. The lack of high-energy data for the strahl allows fewer conclusions for the second power law. Figure 2.6c compares the distribution with that in the reverse direction and makes a fit of their core as a whole and of the suprathermal population for only the counterstrahl. This figure emphasises the enhanced suprathermal population in the antisunward direction of the quasi-parallel distribution. The other distributions of the modified Kappa in the halo and counterstrahl direction having a κ index tending towards infinity $\kappa \to \infty$, the populations are well represented by a Maxwellian. With the distance, the halo expands at the expense of the strahl. (Štverák et al. (2009))

Table 2.2 gives the electron parameters obtained for the Maxwellian + Kappa fit performed on the smaller range of velocity to discard the superhalo. While table 2.3 shows the values obtained with the Olbertian Kappa fit on all the velocities. The uncertainty on

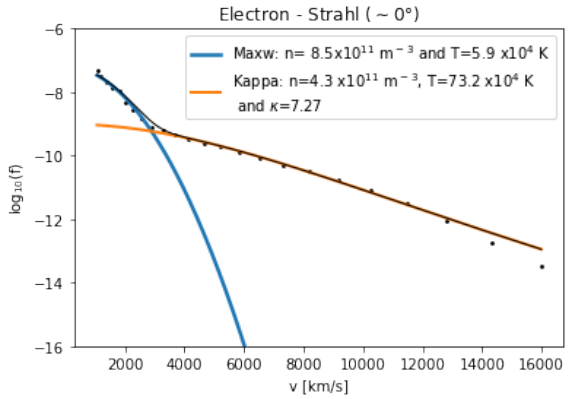

(a) Strahl: Maxwellian and Kappa fit (R^2 of 0.99)

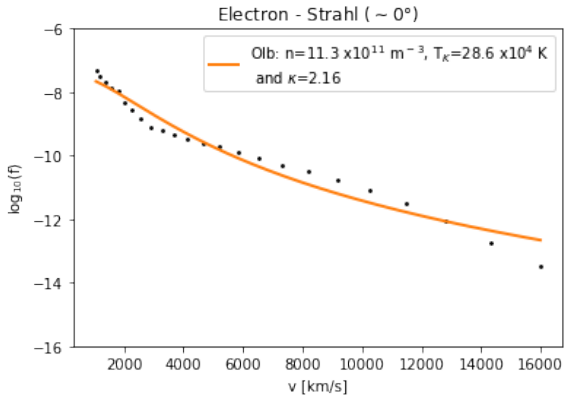

(b) Strahl: Olbertian fit (R^2 of 0.96)

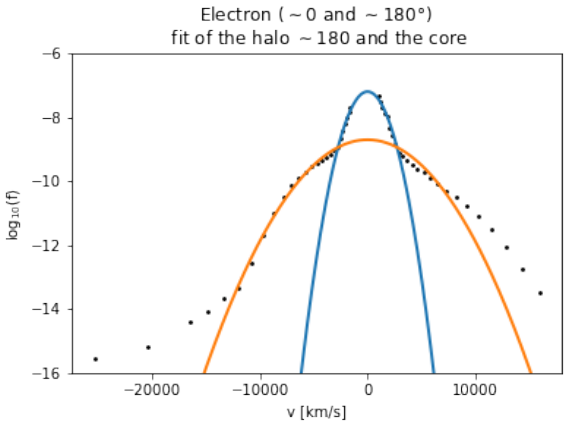

(c) Quasi-parallel distribution: strahl (7.5°) and counter-strahl (172.5°)

Figure 2.6: The black dots are the measured distribution of PSP at a pitch angle of 7.5° (strahl) and in the quasi-parallel plane (7.5° and 172.5°). The blue line is the Maxwellian fit and the orange line is the Kappa fit of the electron distribution.

	$n_c[10^{11}\ m^{-3}]$	$T_c[10^4\ K]$	$n_h[10^{11}\ m^{-3}]$	$T_h[10^4\ K]$	κ	$R^2_{<13000km/s}$
7.5°	8.5 ± 0.9	5.9 ± 0.4	4.3 ± 0.2	73.2 ± 2.4	7.27 ± 1.70	0.995
22.5°	7.1 ± 0.5	4.3 ± 0.3	4.6 ± 0.2	58.0 ± 1.7	10.99 ± 2.27	0.997
82.5°-97.5°	8.0 ± 0.6	4.5 ± 0.2	4.4 ± 0.3	43.8 ± 1.4	118.23 ± 31.1	0.994
172.5°	10.4 ± 0.5	6.3 ± 0.2	5.7 ± 0.7	45.6 ± 3.2	155.98 ± 43.2	0.991

Table 2.2: Parameters of the electrons obtained with a Maxwellian fit for the core and a (modified) Kappa fit for the halo for different pitch angles and for a maximum velocity of 13000 km/s. R^2 is the coefficient of determination. The error on the parameters is the sample variance of the residuals after the fit.

the parameters is the standard deviations of errors. The large error for large kappa values is due to the very small variation of the distribution for large indices. The Olbertian fits have lower values of κ_{Olb} to be able to represent the entire non-thermal population. This fitted index κ_{Olb} has reached its minimum value of 2.16 ± 0.36 in the direction of

	n[10^{11} m^{-3}]	T_κ[10^4 K]	κ	R^2
7.5°	11.3 ± 2.3	28.6 ± 2.9	2.16 ± 0.36	0.960
22.5°	10.9 ± 2.1	25.5 ± 3.1	3.49 ± 0.51	0.969
82.5°-97.5°	11.8 ± 1.7	17.6 ± 1.4	4.22 ± 0.31	0.974
172.5°	10.6 ± 2.5	23.9 ± 3.0	4.79 ± 0.51	0.978

Table 2.3: Parameters of the electrons obtained with an Olbertian Kappa fit for different pitch angles with the coefficient of determination R^2. The error on the parameters is the sample variance of the residuals after the fit.

the strahl. In this direction, a higher temperature is also found. The modified Kappa of the restricted fit has also obtained its smallest κ value in this direction with a higher temperature. Its core properties are however similar to the others. The core density generally constitutes 90-95% of the total density (Maksimovic et al. (2005)). In table 2.2, the obtained core densities seem quite low compared to the suprathermal densities.

2.4.2 Ions

The solar wind ions are dominated by the protons but also consist of some fraction of alpha particles. One can therefore expect to encounter a proton core, proton beams or a population of He^{2+} in the ion VDF.

Figure 2.7 represents fits of proton distribution in a quasi-perpendicular and quasi-parallel direction to the IMF. The blue lines represent as above the Maxwellian distributions and the black dots the distribution observed by PSP. Taking each direction separately, in the halo, strahl and counterstrahl direction, the distribution of the protons in the perpendicular and parallel direction to the IMF are well fitted by a Maxwellian distribution.

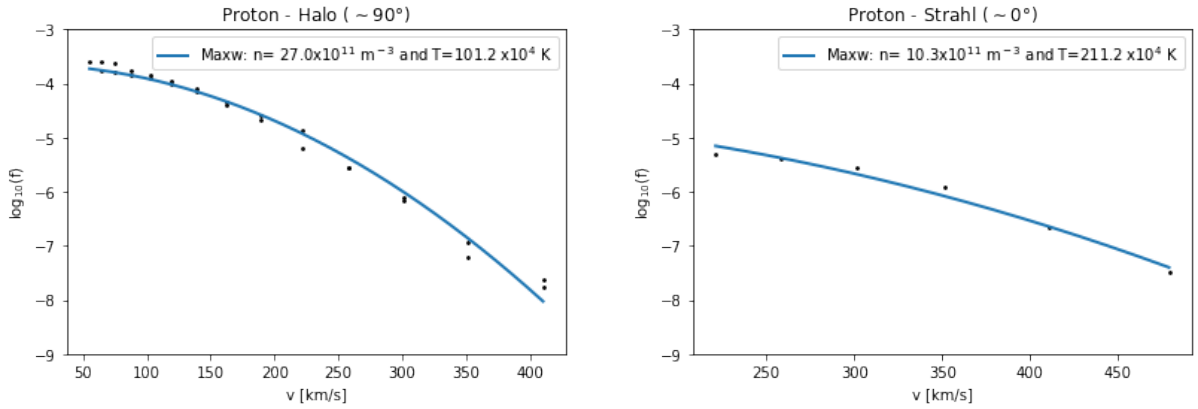

(a) Halo (R^2 of 0.99) (b) Strahl (R^2 of 0.98)

Figure 2.7: Maxwellian fit of the proton VDF at a pitch angle of about (a) 90° and (b) 0°.

However, when one examines the parallel distribution for positive and negative veloci-

ties, one can infer two different populations in a pitch angle close to zero. The fit for representing these two populations is shown in figure 2.8a. The fit for the pitch angle 7,5° cannot be correct otherwise the distribution near 180° would be much higher. The lack of data does not allow to draw any conclusion about the shape of the distribution. Also, due to the lack of data at low positive velocities, it is more interesting to look at a slightly higher angle. One finds again these two distributions in the pitch angle 22° as shown in figure 2.8b.

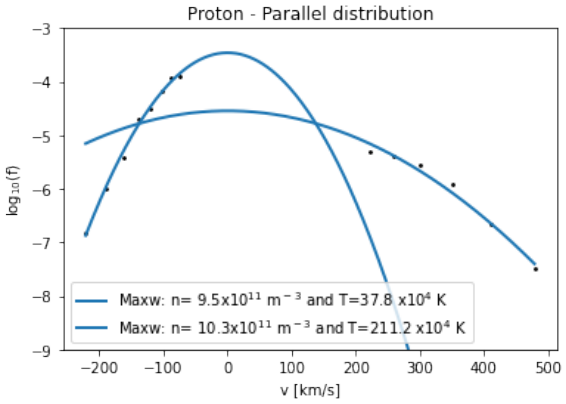

(a) Quasi-parallel distribution (7.5° and 172.5°) (R^2 of 0.71)

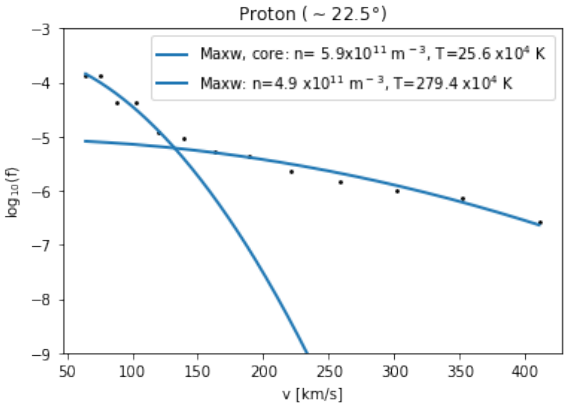

(b) Near the strahl direction (22°) (R^2 of 0.98)

Figure 2.8: Fit of 2 Maxwellians for the distribution in the parallel direction to the IMF and near 22°.

2.5 Discussion

As expected, the ion distribution is characterised by a thermal proton core and by a proton beam or by another population, probably the alpha-particles. With the limited data, no power law can be inferred for the proton distribution at this low distance.
This is not the case for electrons where the electron VDF includes two power laws. The sum of a Maxwellian and a Kappa although very useful to describe the solar wind, is not sufficient. An additional distribution for the superhalo is needed at high energy to properly represent the eVDF. At 17,2 R_S, the high energy particles deviate from the Fokker-Planck solution that considers a Maxwellian distribution.

The Kappa distribution seems only important for electrons. In this distribution, when the analysis was made for the energy range of the halo, only the strahl population needed to be represented by a Kappa distribution. The halo and the counterstrahl could be represented by a second Maxwellian ($\kappa \to \infty$). The strahl, by scattering into the halo, can then affect the electron temperature and the anisotropy for the halo.

The fit is more accurate with a Maxwellian and Kappa sum than a global Kappa distribution (Lazar et al. (2017a)). We need these different populations to accurately represent the whole distribution. However, on a large range of energy, the global

Olbertian distribution better represents the whole distribution than the distribution of the sum of a Maxwellian and a modified Kappa. The distribution of the superhalo must be added. However, care must be taken that the distribution does not account for superluminal particles ($v > c$). The good representation is a positive result for the use of the Olbertian function in exospheric models. Thus, the assumption of this Kappa distribution at the exobase is relevant.

The superhalo is observed quasi-isotropic and with density values between 10^{-8} and 10^{-5} cm^{-3} (Wang et al. (2015)). This population being present during periods of quiet solar activity, the high speed of this population cannot be due to an energy event (Wang et al. (2012)). It seems to be present in all conditions of solar activity. Therefore, it may be assumed that this population is rather due to wave-particle interactions. Kim et al. (2016) showed that the superhalo is in resonance with the Langmuir frequency range.

The suprathermal population of the eVDF is important for the calculation of the electric field and heat flux as seen in the previous chapter. At all pitch angles, the Olbertian Kappa model fits large tails with an associated low κ. In this case, the kappa values are not so far from 2. As a reminder from chapter 1, in the kinetic approach, the kappa value must satisfy $\kappa > (l+1)/2$ to be able to obtain a moment of order l. Regularized Kappa distributions have thus been developed to avoid the divergence of the moments, as we will explain in more details in Chapter 4.

Lazar, M., Fichtner, H., and Yoon, P.H. (2016) showed that the modified Kappa and Olbertian distributions were both valid but for specific interpretations. However, being less specific to a physical interpretation, Lazar, M., Fichtner, H., and Yoon, P.H. (2016) conclude that the Olbertian distribution should be used more. Lazar et al. (2017b) show that the Olbertian distribution is the only distribution that, from a temperature anisotropy of the suprathermal particles, can systematically induce instabilities. Instabilities such as firehose instability for $A_{halo} = T_{h,\perp}/T_{h,\parallel} < 1$ and electron cyclotron (whistler) instability for $A_{halo} = T_{h,\perp}/T_{h,\parallel} > 1$ are generated by this temperature anisotropy. These instabilities lead to wave-particle interactions. The pitch angle scattering phenomenon is probably related to this kind of interaction.

Chapter 3

Link between solar wind parameters

3.1 Introduction

The purpose of this chapter is to understand how parameters of the solar wind are related to each other, especially at low distances. The exospheric model considers that there are no interactions above the exobase. As discussed in the previous chapter, there are probably wave-particle interactions that impact the distribution. There may also be particle-particle interactions. Relations between the different populations of the VDFs or between the macroscopic quantities may help to understand some of the processes that form the velocity distributions near the Sun.

In this way, such links can be useful for solar wind models by making more accurate predictions at greater distances. It can also indicate the most suitable conditions that can be used for models where a density, a temperature,... are chosen for the exobase. The focus will be on protons and electrons. Electrons play a critical role in the heat flux and the dynamics of the plasma, while protons with their larger mass will be involved in the bulk of the solar wind.

3.2 Data

This chapter is centred on the analysis of data collected by PSP, SolO, Ulysses (UY) and from the High-Resolution OMNI data set. OMNI is a database of solar wind magnetic field and plasma data around the Lagrange point L1, located at 1.5 million kilometres from the Earth in the direction of the Sun. In the time range studied, the data from OMNI are from the spacecraft missions Wind and ACE (Advanced Composition Explorer).

The chosen time range correspond to the PSP dataset. Data of other spacecraft are also available on this time, except for Solar Orbiter that was launched in 2020 and Ulysses that was launched in 1990 but ended on 30 June 2009 and is useful for observations at large distances. Therefore, to be able to compare with a similar period in terms of energetic events, the time period of Ulysses was taken close to a minimum of solar activity, while electron temperatures from the spacecraft were still available.

To analyse only data near the solar ecliptic plane, like for PSP, the data of Ulysses were restricted to a HelioGraphic Inertial (HGI) latitude of $[-15° : 15°]$. The solar ecliptic makes an angle of 7.25° with the solar equatorial plane. Table 3.1 gives the time interval, the distance observed, the latitude, the size of the sample for each mission. The distance range are expressed in AU unit, i.e. the distance between the Sun and the Earth.

Satellite	Time interval	Distance (AU)	Latitude range (HGI)	Samples
PSP	15/10/2018-12/11/2021	0.08 to 0.80	$[-4.1° : 4.1°]$	≈5000
Solar Orbiter	07/07/2020-14/08/2021	0.59 to 0.99	$[-6.7° : 3.8°]$	≈ 29000
OMNI data set	15/10/2018-12/11/2021	0.97 to 1.01	in ecliptic plane	≈ 301000
Ulysses	01/01/1995-31/12/1996	1.34-1.36	$[-15° : 15°]$	≈900

Table 3.1: The observation periods, distance ranges from the Sun, the solar ecliptic latitude ranges and the number of data from Parker Solar Probe, Solar Orbiter, the database OMNI and Ulysses.

For the electron data, Ulysses is the only spacecraft that gave information on the total, core and halo electron density and temperature. From PSP, only the electron number density and the electron core temperature are obtained from a simplified analysis of the plasma quasi-thermal noise (QTN) spectrum with the Radio Frequency Spectrometer (FIELDS). The description of the first in situ measurements with PSP/FIELDS are described in Moncuquet et al. (2020). Moncuquet et al. conclude that measurements obtained via QTN are in broad agreement with the results from the Solar Probe Analyzer (SPAN) on SWEAP. The other spacecraft provide only the proton density, proton temperature and bulk speed.

PSP and UY data are downloaded from the NASA CDAWeb: `https://cdaweb.gsfc.nasa.gov/`. OMNI data are from the interface OMNIWeb: `https://omniweb.gsfc.nasa.gov/form/omni_min.html`. The Solar Orbiter data comes from the ESA Solar Orbiter Data Archive at `http://soar.esac.esa.int/soar/`. The radial distance of OMNI and Solar Orbiter were, however, obtained by CDAWeb. The distance Earth-Sun from DSCOVR (from CDAWeb) was used to obtain the distance of OMNI from the Sun.

3.3 Analysis of the parameters

The data are taken during low solar activity. In this situation, the coronal holes appear more at high latitude and CMEs and solar flares are rare. These in-situ data are from low latitude. It is therefore expected to see more slow wind that is more variable and is more associated with a higher density. As explained in Chapter 1, the fast solar wind is assumed to come from coronal holes (Cranmer (2002)), regions characterized by a lower electron temperature and a lower proton and electron density than other regions of the corona.

Due to the lower thermal velocity of proton $v_{th,p}$, the bulk velocity of protons is easier to estimate than the bulk velocity of electrons. However, the bulk velocities of the

protons and the electrons must be close due to the zero-current condition to satisfy the quasi-neutrality. As a consequence, the correlation analysis is easier for the protons.

3.3.1 Protons

Figure 3.1 illustrates the radial profile of the proton bulk speed, proton temperature and proton density measured by PSP. The data were divided into intervals by radial distance. The black lines correspond to their arithmetic mean and the vertical black lines to their standard deviation. The bulk velocity for the different spacecraft has values between 200 km/s and 840 km/s.

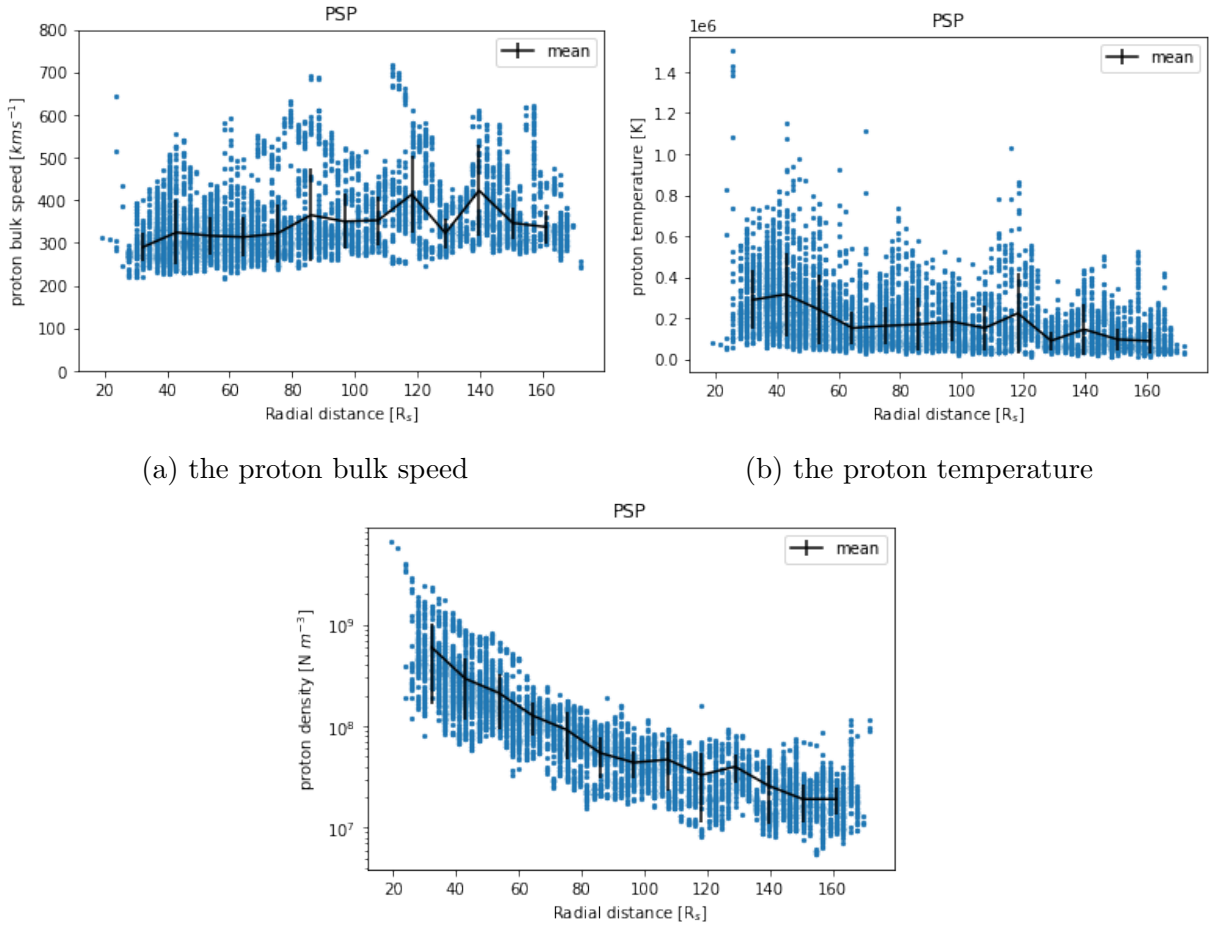

(a) the proton bulk speed

(b) the proton temperature

(c) the proton density

Figure 3.1: The radial profile of (a) the proton bulk speed, (b) the proton temperature and (c) the proton density observed by PSP. Measured data are in blue, the black line corresponds to the averaged values as a function of the distance and the black vertical lines correspond to the error bars calculated using standard deviation.

A correlation between the proton temperature and the bulk speed has been reported widely in the literature (Burlaga, L.F. and Ogilvie, K.W. (1970), Arya, S. and Freeman,

J. W. (1991), Matthaeus, W. H., Elliott, H. A., and McComas, D. J. (2006) Watari (2018), Pierrard, V., Lazar, M., and Štverák, S. (2020)). This link is still not well understood. This is probably related to Alfvenic fluctuations or turbulent energy cascade. However, some information about this relationship is known.

First, this relationship is not obtained during CMEs (Matthaeus, W. H., Elliott, H. A., and McComas, D. J. (2006)). At this time, low-temperature values can be observed for high velocities. This relationship is therefore useful for the identification of these phenomena. For a more accurate study, the data associated with CME should be removed. However, since the data are in a minimum of solar activity and the low-temperature data for the high velocity are weakly observed, the following analyses remain valid. Also, to take account of the compression phenomenon during shock front that can increase the temperature, a separation between compressed and non-compressed data ("rarefaction") would be interesting as a deepening of the analysis.

Next, Elliott et al. (2012) showed that linear fits were best suited for the $T_p - v$ relationship. By studying this relationship at several distance intervals from 0.29 to 5.4 AU, Elliott et al. (2012) observed that this link, in the case of compression, was deviated after 2.5 AU. They were also able to show that the slope of the relationship $T_p - v$ decreased between 1972 and 2010 and increased again between 2010 and 2016 (Elliott, H.A., McComas, D. J., and DeForest, C.E. (2016)). Varying with the solar cycles, the slope increases when the solar wind pressure and the magnetic field intensity increase.

The relationship is studied here at various intervals of radial distances. Figure 3.2 shows the proton temperature as a function of the proton bulk speed obtained by PSP and Solar Orbiter at different distance intervals including the one where the PSP and Solar Orbiter data match. The linear regression line is shown in red. The points are more spread out in the figure 3.2a. Since the slope may vary with radial distance, it is probably due to to the larger distance interval.

Indeed, table 3.2 gives the slope a, the intercept b and Pearson correlation factor for the linear regression equation, $T_p = aV_{SW} + b$, at various distance ranges having a certain amount of data N for the different satellites. It shows that the correlation remains apparent at ranges of distances between 0.09 AU to 1.38 AU. However, the correlation coefficient stays relatively high only when we keep the distance interval relatively small. Except for 80 to 110 R_S interval, the slope of the linear regression seems to decrease with the heliocentric distance. With the profiles of the figure 3.1, the variation of the slope is not a surprising feature. There is a small increase in velocity while the temperature of the proton varies by a larger order of magnitude

With this correlation, it is therefore not surprising that the density of the solar wind has a similar relation to the velocity of the proton and its temperature. Figure 3.4 shows the proton density as a function of the bulk speed for the different spacecraft and different distance ranges. One can see that the link of density with velocity (or temperature) has a two-branch effect: a high-density effect and a low-density effect. The proton density is high only for low bulk velocity (or low temperature) while a low proton density is

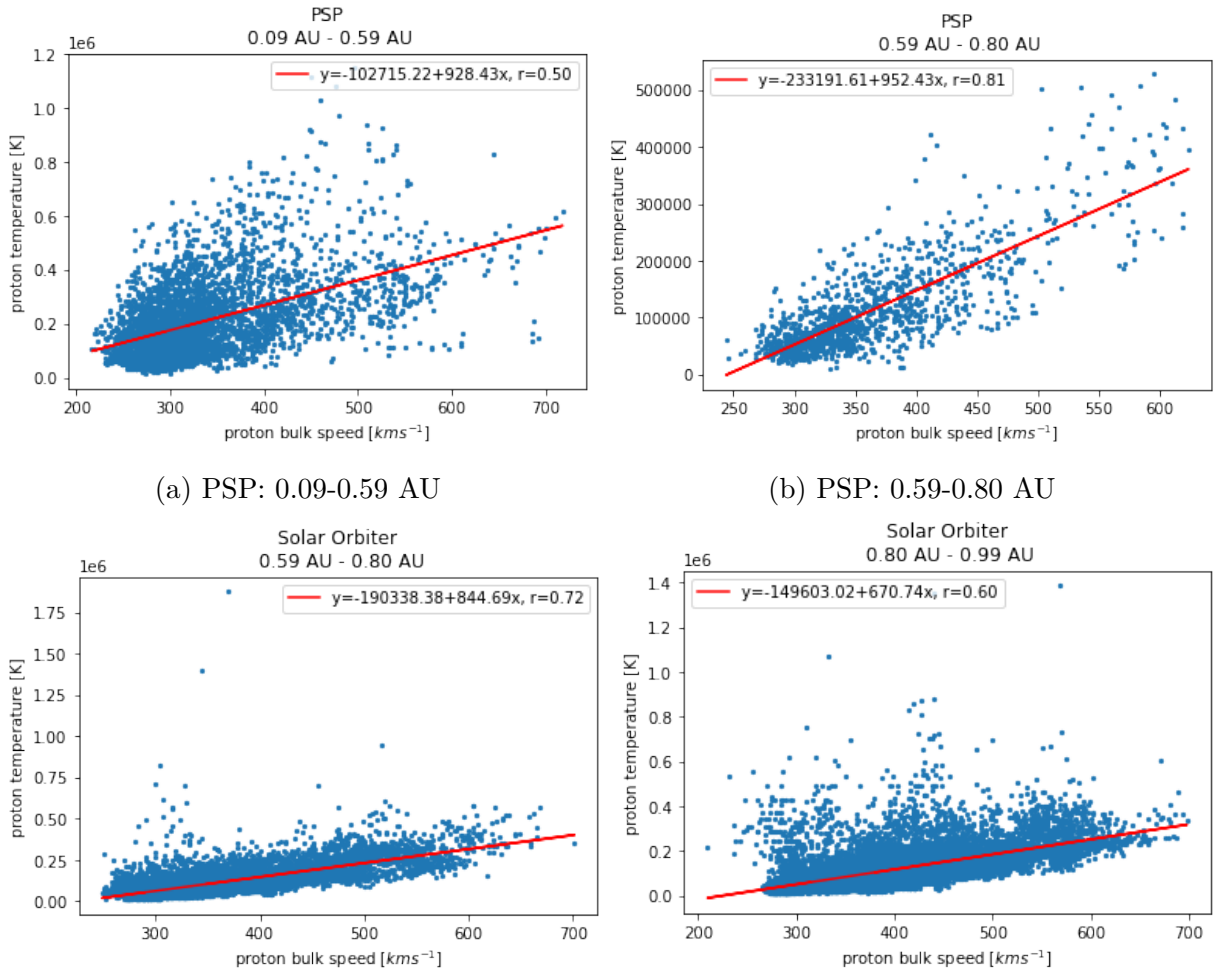

(a) PSP: 0.09-0.59 AU

(b) PSP: 0.59-0.80 AU

(c) SolO: 0.59 - 0.8 AU

(d) SolO: 0.80-0.99 AU

Figure 3.2: The proton temperature as a function of the proton bulk speed from Parker Solar Probe and Solar Orbiter on distance intervals 0.09 - 0.59 AU, 0.59 - 0.80 AU and 0.80-0.99 AU. The red line represent the regression line.

compatible with all bulk speeds.

Fast solar winds coming from coronal holes are associated with a low density (Cranmer (2002)). It is expected to see a higher density at low speeds. Looking over a large distance interval, it is normal to see lower densities since the density decreases with altitude. However, the very low high? proton density related with the slow solar wind is probably due to the shock front when fast solar winds catch up with slow solar winds. The compression creates a high-density peak that then decreases with an increase in velocity. Considering this explanation, it can be deduced that the shock front can be formed at lower distances than 30 R_S. Indeed, figure 3.3 shows the density as a function of the velocity measured by PSP for a maximum altitude of 30 R_S and 40 R_S. These high and low densities associated with a low speed are already observed below 30 R_S. This front can then evolve and be present at a greater distance. This two-branch relationship is less apparent at greater distances as can be seen in the figure 3.4.

	distance (R_S)	a (K s/km)	b (K)	r	N data
PSP	19.4 to 50	1886	-31.0 $\times 10^4$	0.71	1287
	50 to 80	1186	-31.0 $\times 10^4$	0.61	1452
	80 to 110	801	-14.0 $\times 10^4$	0.68	949
	110 to 140	1165	-28.0 $\times 10^4$	0.78	807
	140 to 172.2	988	-25.0 $\times 10^4$	0.82	921
SolO	126.8 to 172	847.83	-19.2$\times 10^4$	0.72	13603
	172 to 212.8	670.73	-14.9$\times 10^4$	0.60	15812
OMNI	209.3 to 216.6	542.94	-14.6$\times 10^4$	0.73	297687
UY	288.0 to 296.6	530.30	-15.5$\times 10^4$	0.76	916

Table 3.2: The parameters of the correlations between the proton temperature T_p and bulk speed V_{SW}. The equation of the linear regression is $T_p = aV_{SW} + b$ with a the slope, b the intercept of the regression line, r the linear Pearson correlation factor and N the number of data in this analysis. The values are calculated with the least-squares method.

As said above, in compression events, the slope of the temperature-velocity relation is greater than in rarefication events. Thus, with this compression at a low distance that can be assumed with the figure 3.3, a greater slope can be obtained if more rarefactions occur in the other distance intervals.

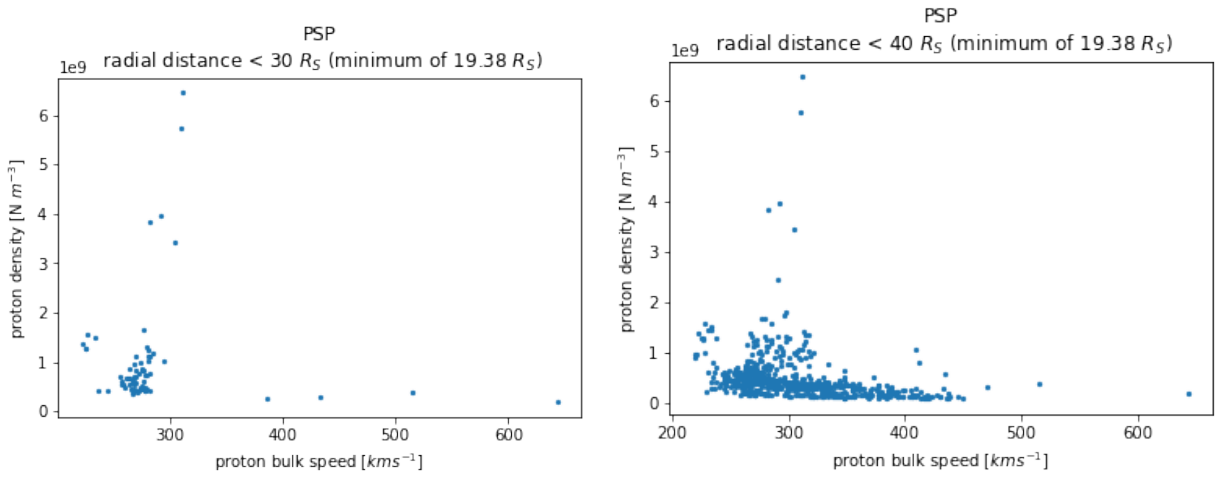

(a) 19.38 - 30 R_S

(b) 19.38 - 40 R_S

Figure 3.3: The proton bulk speed as a function of the number density of protons from the mission PSP on different distance intervals.

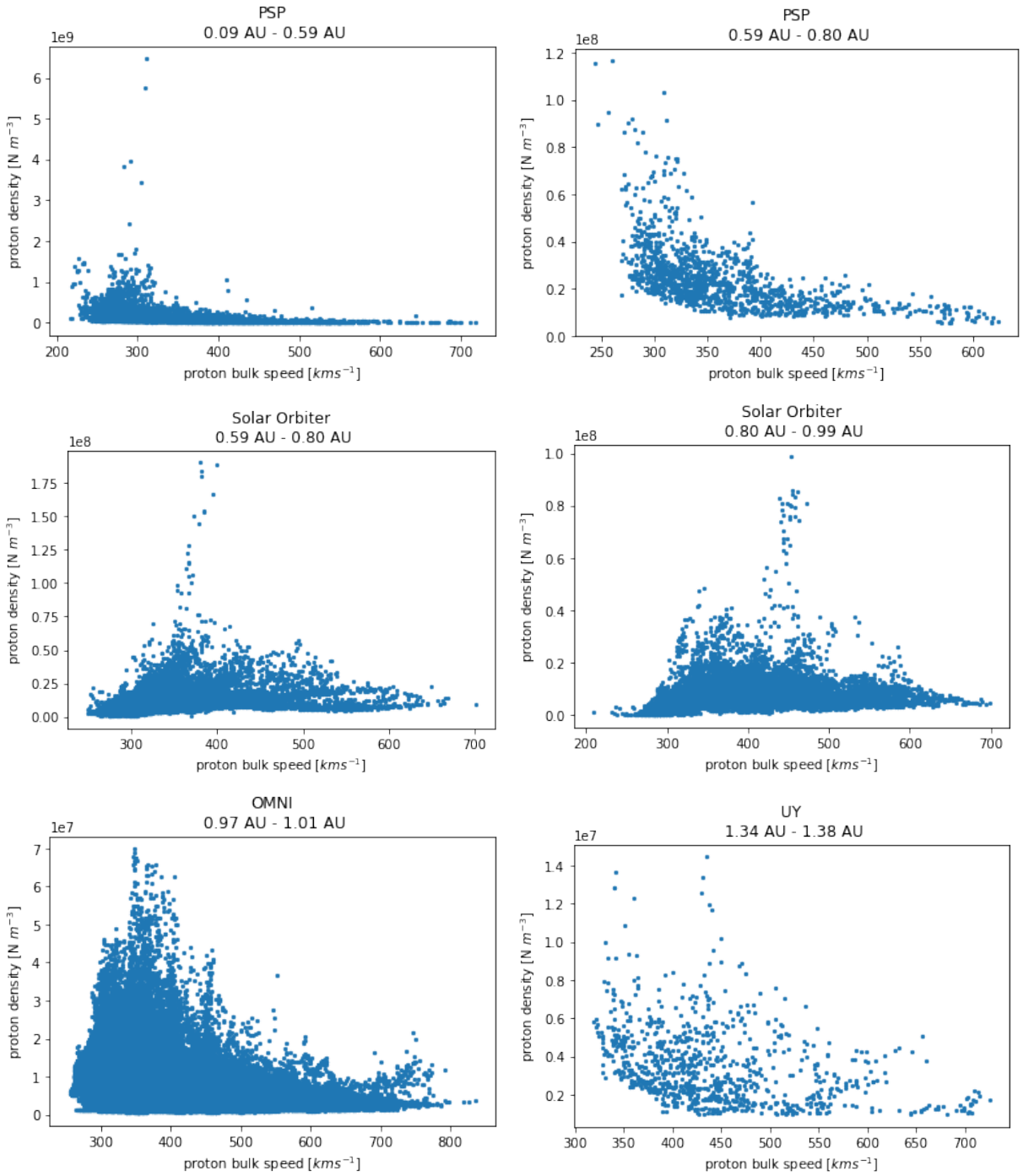

Figure 3.4: The proton bulk speed as a function of the number density of protons from the missions PSP, SolO, OMNI and UY.

3.3.2 Electrons

Due to the limited available data on the electrons from PSP, a similar study to that of protons cannot be made here. However, some links obtained from the first orbits of the PSP mission can be found in the literature (e.g: Halekas et al. (2020), Berčič et al. (2020), Maksimovic et al. (2020))

Figure 3.5 shows the radial profile of the electron core temperature and the electron density from 0.11 to 0.6 AU. Figure 3.6 shows these two parameters as a function of the bulk speed.

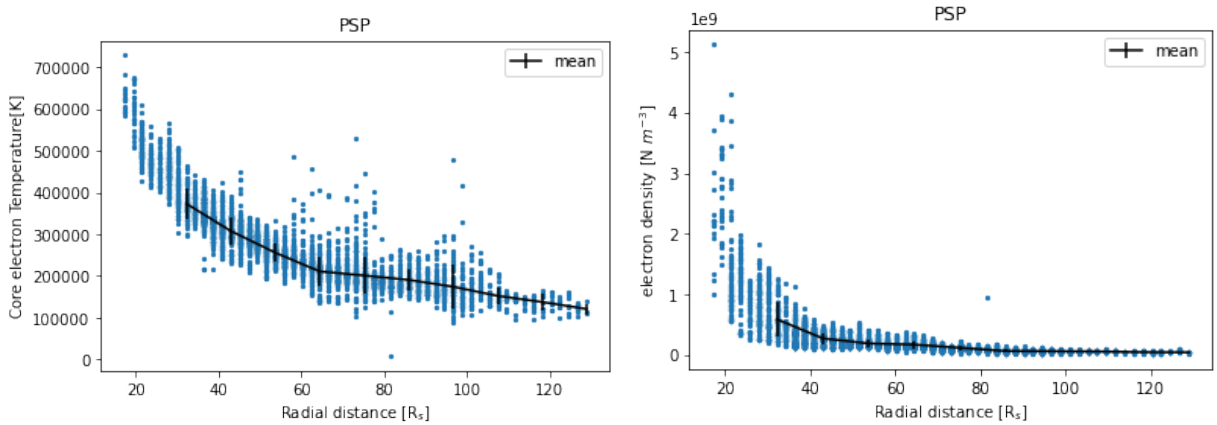

(a) Electron core temperature (b) Electron density

Figure 3.5: The radial profile of (a) the electron core temperature and (b) the electron density measured by PSP. Data are in blue, averaged values in black, error bars correspond to the black vertical lines.

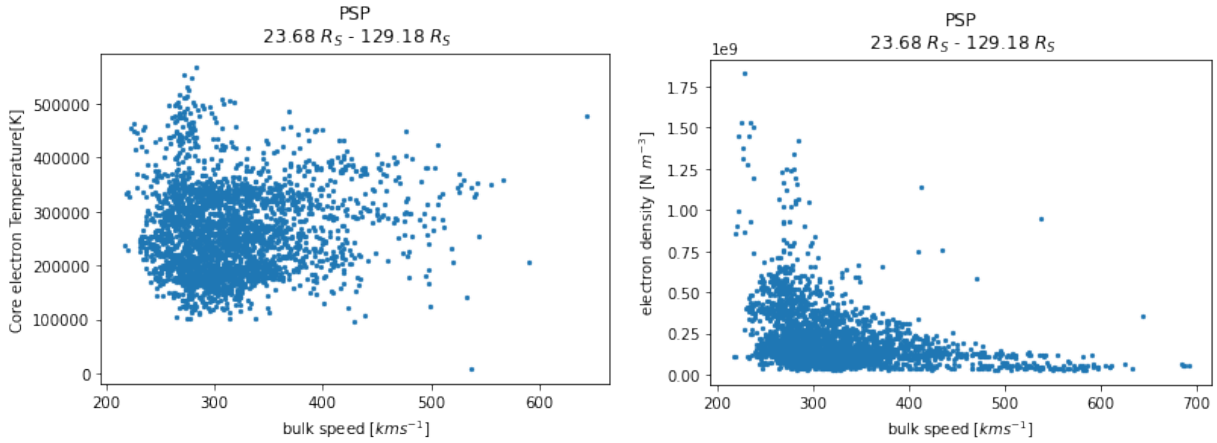

(a) Electron core temperature (b) Electron density

Figure 3.6: (a) The electron core temperature and (b) the electron density of PSP as a function of the bulk speed of the solar wind.

Given the quasi-neutrality and that the ions of the solar wind are mainly protons, it can be expected that electrons have the same relation for the density with the bulk speed as the protons. Indeed, figure 3.6b shows the same relationship as with the proton from 0.11 to 0.6 AU. Pierrard, V., Lazar, M., and Štverák, S. (2020) have shown that the anti-correlation between the density of the core electrons and the bulk speed becomes weaker with distance but is still apparent at 1 AU. Lazar et al. (2020a) also showed an

anti-correlation under 1 AU that decreases with distance between the bulk speed and halo parameters including the density.

Concerning the temperature, figure 3.5a shows that the electrons of the core have a temperature that decreases with altitude. A result also obtained by Halekas et al. (2020). Pierrard et al. (2016) have also observed this decrease with a slightly increase of the halo temperature with distance from 0.3 to 4 AU in the ecliptic.

As can be deduced from figure 3.6a, no correlation was observed between the bulk speed and the core temperature of electrons even when looking at smaller distance intervals. However, few data are available for fast winds and, in contrast, an anti-correlation between these two parameters was observed by Pierrard, V., Lazar, M., and Štverák, S. (2020) using Helios data mainly. For the halo, Lazar et al. (2020a) show an anti-correlation between the bulk speed and the halo temperature. The anti-correlation between the total electron temperature and the bulk speed was also found at distance as small as 0.17 AU (Maksimovic et al. (2020), Halekas et al. (2020)). But the latter relationship disappears as the radial distance increases, when the solar wind evolves, accelerates, and mixes. Thus, the electron temperature cools faster with the radial distance for slow solar wind than fast solar wind (Maksimovic et al. (2020)). The anti-correlations then indicate that the signatures of the solar wind sources remain visible in the electron distributions at distances close to the Sun.

This anti-correlation was also found for the strahl temperature in the parallel direction and was found to be constant with radial distance (Berčič et al. (2020)). This suggests that the strahl parallel temperature carries the information on the electron temperature of the corona. More analysis is needed to confirm this assumption.

The fast solar wind is typically associated to a low kappa (Maksimovic et al. (2005), Pierrard et al. (2016)). The associated lower density from coronal holes makes collisions rarer, resulting in a lower kappa value involving larger suprathermal tails. It is the highly energetic electrons that are the ones responsible for the acceleration of the solar wind in the kinetic model (Scudder (1992a),Scudder (1992b),Zouganelis et al. (2005)). However, the acceleration is mainly a consequence of the anisotropic strahl which accounts for most of the suprathermal particles at low altitudes (Halekas et al. (2020)).

Indeed, the ratio of suprathermal electrons ($n_h + n_s$) to the core (n_c) is relatively constant with radial distance (Štverák et al. (2009)). The energetic electrons are thus already present at low distances. But from 0.3 to 4 AU, the density of the halo increases at a rate comparable to the decrease in density of the strahl (Štverák et al. (2009)). This suggests a mechanism that scatters electrons from the strahl to the halo with the distance (Maksimovic et al. (2005), Štverák et al. (2009)). At lower distances, down to 0.17 AU, the density of the strahl is higher and the diminishing halo reaches a plateau as it approaches the Sun (Halekas et al. (2020)). The strahl dominates the suprathermal electrons near the Sun and becomes narrower reaching down to a pitch angle width of 30° at 35 R_s (Berčič et al. (2020)).

3.4 Discussion

Relations close to the Sun, that are not observed at greater distances, are interesting for the understanding of the processes that affect velocity distributions of the solar winds. A lot of characteristics of solar wind have trends with the bulk speed. These trends may provide information on the assumed distinct origin of the slow and fast solar winds.

For the study of solar wind parameters, it is relevant to use the temperature anisotropy. The temperature anisotropy provides clues on the mechanisms playing on the distribution of the solar wind particles. Štverák et al. (2008) have shown that plasma instabilities and Coulomb collisions are associated with the isotropization mechanisms. Indeed, by deviating from the isotropy, this can induce instabilities. In order to overcome them, fluctuations are generated which minimize the anisotropy through pitch-angle diffusion.

In the shocks, following the compression, an increase in the proton temperature, the magnetic field intensity, the density and the solar wind speed is observed (Melkumyan et al. (2020)). Thus, one can expect to observe links between these parameters. It is therefore interesting to study the wind with the beta plasma β, the ratio of the plasma pressure to the magnetic field pressure.

With data from different satellites, a linear relationship between proton temperature and bulk velocity was found at distances from 0.08 to 1.36 AU in the ecliptic. However, the slope of the relationship changes with distance and solar activity. Compression events, the activity of the Sun and the distance to the Sun can therefore impact the relationship. The non-linear relationship between density and velocity could also be observed at all distance intervals.

For the electron temperature (total and halo), it is an anti-correlation with the global velocity that has been observed in the literature (Maksimovic et al. (2020), Lazar et al. (2020a)). This link was also observed for core temperature at 0.4 AU and 1 AU. However, no link was observed in our analysis at distances from 0.11 to 0.6 AU probably due to a lack of high-speed data.

The fast solar wind, associated with colder coronal holes, has typically lower densities and lower electron temperatures. However, this link with weak electron temperatures disappears at 1 AU when the solar winds mixes and expands. Thus, the ratio of the electron to the proton temperature has then a strong anti-correlation with the velocity close to the Sun (Halekas et al. (2020)). The anti-correlation between the temperatures of proton and electron at small distances is surprising and not understood. Near the Sun, in the slowest solar wind, the temperature of the electrons is higher than that of the proton. The opposite is observed in the strongest wind (Halekas et al. (2020)).

Finally, close to the Sun, the suprathermal electrons are dominated by the strahl population. The halo is there almost absent (Halekas et al. (2020)). The strahl parallel temperature $T_{s,\parallel}$ could transport information on the electron temperature of the corona. If the spread of the solar wind was adiabatic, by conservation of magnetic moment,

one would observe at 1 AU a strahl centred on a small angle, the magnetic field being weaker than near the Sun. The temperature parallel to the IMF would be much more important than the perpendicular temperature. By observing pitch-angles of all widths, a scattering process acts on the eVDF and is probably due to wave-particle interactions.

Pierrard et al. (2016) showed that for low values of the κ-index, the core and the halo deviate in the same direction. The thermalization is therefore probably due to Coulomb collisions and fluctuations. This suggests that the different populations of the electron VDF should not be studied separately but collectively. As discussed in Chapter 2, the use an Olbertian distribution with a κ-dependent temperature is more appropriate for kinetic instability study.

Chapter 4

Comparison in-situ data and exospheric model

4.1 Introduction

Now that the presence of the suprathermal population and the link between the solar wind macroscopic quantities were discussed, the kinetic model can now be addressed.

By studying the Olbertian Kappa functions in chapter 2, one observed the relevance of considering exospheric models that allows calculation even for low kappa values. Using the regularised Kappa function, it is now possible to calculate the moments for all values of the index $\kappa > 0$ (Scherer, K., Fichtner, H., and Lazar, M. (2017)). This distribution has been implemented in a pre-existing exospheric model. The following chapter focuses on the comparison of the results of the improved exospheric model with in-situ data from several satellites.

4.2 The exospheric model

As explained in Chapter 1, the exospheric model is a simple model that calculates several properties of the solar wind. It assumes that there are no collisions above the exobase. With the VDF of the particles assumed at the exobase, one can calculate the moments at any higher altitudes. The input parameters are thus the proton and electron temperature at this altitude, a kappa index, and a final altitude. The model used in this chapter considers a non-rotating exosphere. This remains a valid model as the Parker spiral structure does not affect the moments significantly except for particle temperatures (Pierrard et al. (2001)). The effect on the temperature will be discussed below. The exobase is considered to be at the same height for the proton and the electrons. This assumption is valid only when the protons and electrons have the same temperatures. However, the temperature of protons is observed to be usually higher than that of electrons.

The model used here is based on the equations of the Lorentzian ion exosphere of Pierrard, V. and Lemaire, J. (1996) and on the non-monotonic proton potential of Lamy

et al. (2003). The model only considers electrons and protons and not the other ions.

The suprathermal particles are only important for the electrons so the assumption that the proton VDF is Maxwellian is appropriate. As discussed in Chapter 1, suprathermal electrons significantly impact the heating and acceleration of plasma by contributing to the electron heat flux and influencing the generation of the electric field along open magnetic flux tubes. The VDF of the electrons in the initial model is considered to be an Olbertian Kappa distribution.

4.2.1 Improvement of the model

As discussed in Chapter 1, in order to ensure non-divergent moments of order l, the critical limitation $\kappa > (l+1)/2$ must be respected. Thus, to define the heat flux, that is crucial in exospheric models, the κ parameter must be $\kappa > 2$. With the modified Kappa distribution or the Olbertian Kappa distribution, the moment start to diverge for $\kappa \leq 2$ for truncated distributions and for $\kappa < 3/2$ for the temperature even for isotropic distributions. As a reminder, a moment of order l is of the following form :

$$M^{(n)} \sim \int_{-\infty}^{\infty} (\mathbf{v}-\mathbf{u})^{(n)} f(\mathbf{r},\mathbf{v},t) d^3\mathbf{v} \tag{4.1}$$

and moments are well defined by the equations 1.3-1.7.

Scherer, K., Fichtner, H., and Lazar, M. (2017) introduce the regularized Kappa distribution (RKD) to solve this limitation. This distribution is expressed as followed :

$$f_R(\kappa, v) = nN_R \left(1 + \frac{v^2}{\kappa\theta^2}\right)^{-\kappa-1} e^{-\alpha^2 v^2/\theta^2} \tag{4.2}$$

where $0 < \alpha < 1$ is the cut-off parameter and N_R is a normalized constant.

This change has also physical explanations. First, the divergence of moments made a hydrodynamic description impossible. Also, the previous Kappa distributions involved non-extensive entropy. At last, contrary to the exponential tails of the Maxwellian, the power laws for relatively low kappa are non-negligible at velocities higher than the speed of light in the vacuum c. To solve the latter problem, an appropriate α and θ factor is needed to obtain a proper cut-off of the distribution that excludes velocities unreasonably large.

Figure 4.1 illustrates the Olbertian distribution for a $\kappa = 2$ (solid red), the corresponding RKD for an $\alpha = 0.2$ (dashed line blue) and the Maxwellian distribution (dashed line black). The Olbertian distribution is equivalent to the RKD distribution with a value of $\alpha = 0$. This shows that a RKD distribution with $\alpha > 0$ reduces the tail by approaching the Maxwellian limit. To avoid the contribution of superluminal particles that has speed values above the speed of light to the moments, Scherer et al. (2019b) showed that a value α must satisfy $\alpha > \theta/c$. With these requirements, Lazar et al. (2020b) determined a value of $\alpha = 0.012$ using solar wind conditions obtained at 1 AU. This alpha value will

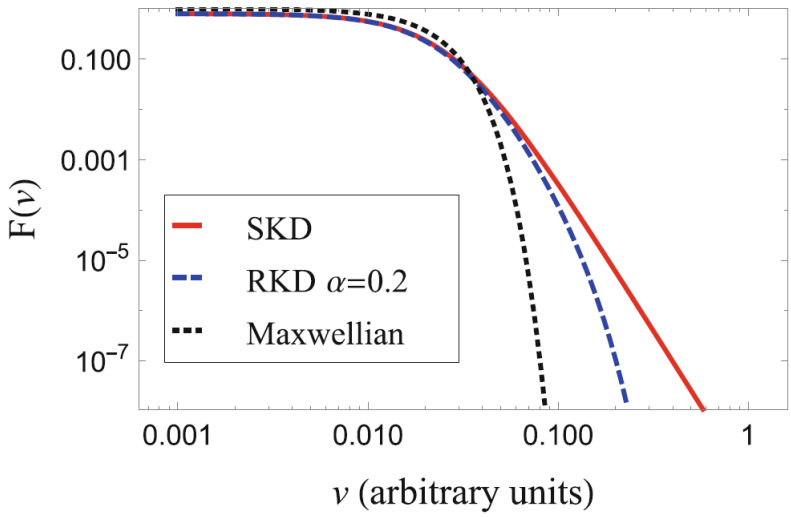

Figure 4.1: Comparison of the Olbertian Kappa distribution (SKD, in red), the regularized Kappa distribution (RKD, in blue) for a $\kappa = 2$ and the Maxwellian limit $\kappa \to \infty$ (black). Source: Fichtner and Lazar (2021)

also be used here.

The consideration of this distribution makes the calculation of moments possible for any $\kappa > 0$. Also, the entropy, a thermodynamic quantity not calculated by the model, is with this change now correctly described (Fichtner et al. (2018)).

To define the normalized constant N_R, Scherer et al. (2019a) have introduced the function ${}_{[m]}\mathscr{U}_{[n]}(\kappa, \alpha)$ that is a ratio of two Kummer (or Tricomi) functions U. It will allow the representation of moments with the distribution $f_R(\kappa, \alpha)$. This ratio is expressed as follows:

$$ {}_{[m]}\mathscr{U}_{[n]}(\kappa, \alpha) = \frac{U(\frac{3+m}{2}, \frac{3+m}{2} - \kappa, \alpha^2\kappa)}{U(\frac{3+n}{2}, \frac{3+n}{2} - \kappa, \alpha^2\kappa)} \tag{4.3} $$

The table 2 of the article of Scherer et al. (2019a) gives the moments for the isotropic non-drifting distribution function. This table permits to deduce how to make the transition between the standard isotropic kappa distribution $f_K(\kappa)$ as defined in equation 2.2 to the regularized Kappa distribution $f_R(\kappa, \alpha)$ for each moment. Table 4.1 shows how different moments are modified by a change in distribution.

By applying these changes in the initial exospheric model, one can finally obtain the different macroscopic quantities for $\kappa < 2$. Figure 4.2 shows the moments from the modified model for κ indices ranging from 1,8 to 2,1. At values of $\kappa \geq 2$, the regularized Kappa distributions give the same moments as the Olbertian Kappa.

	$f_R(\kappa, \alpha)$	$f_K(\kappa)$	f_M
n	$_{[0]}\mathscr{U}_{[0]} \frac{1}{(\pi\kappa\theta^2)^{3/2}}$	$\frac{1}{(\pi\kappa\theta^2)^{3/2}} \frac{\Gamma[\kappa]}{\Gamma[\kappa-1/2]}$	$\frac{1}{(\pi\theta^2)^{3/2}}$
u	$_{[1]}\mathscr{U}_{[0]} \frac{2\theta\sqrt{\kappa}}{\sqrt{\pi}}$	$\frac{2\theta\sqrt{\kappa}}{\sqrt{\pi}} \frac{\Gamma[\kappa-1]}{\Gamma[\kappa-1/2]}$	$\frac{2\theta}{\sqrt{\pi}}$
P_{11}	$_{[2]}\mathscr{U}_{[0]} \kappa \frac{n_0\theta^2}{2}$	$\frac{n_0\theta^2}{2} \frac{\kappa}{\kappa-3/2}$	$\frac{n_0\theta^2}{2}$
q	$_{[3]}\mathscr{U}_{[0]} \frac{4n_0(\kappa\theta^2)^{3/2}}{\sqrt{\pi}}$	$\frac{4n_0(\kappa\theta^2)^{3/2}}{\sqrt{\pi}} \frac{\Gamma[\kappa-2]}{\Gamma[\kappa-1/2]}$	$\frac{4n_0\theta^3}{\sqrt{\pi}}$

Table 4.1: The moments for non-drifting isotropic distribution functions including the regularized Kappa f_R, the Olbertian f_K and the Maxwellian f_M distributions. The moments are the number density n, the most probable speed u, the pressure component P_{11} ($P_{11} = P_{22} = P_{33}$) and the most probable heat flux q. The equations are obtained from Scherer et al. (2019a).

Profiles of the moments

Figure 4.2 illustrates well the mechanism of the solar wind acceleration explained in the introduction. When the kappa index has a smaller value, the suprathermal tails of the electron distribution are higher, leading to a higher flux. It produces a greater polarisation electric field that will generate a higher proton flux to keep the solar wind quasi-neutral. The bulk speed is therefore increased. The model explains why one finds mainly fast winds with a lower kappa index. With these initial conditions, a kappa of $1,8$ even exceeds a bulk speed of 1000 km s^{-1}. The moments of the protons do not change significantly with the different κ since their VDF is Maxwellian. Its flux is increased but its Maxwellian distribution remains the same.

One observes that the electron temperature has a maximum. This maximum is higher when the κ index is lower. By increasing the index, the temperature profile will no longer have a maximum. The model represents well the temperature inversion.

Being the main particles of the solar wind, protons and electrons define the electrostatic potential. The other ions do not have a significant impact. Hence protons and electrons have the same bulk speed. The bulk speed is strongly accelerated before tending towards an approximately constant value. A higher bulk velocity is achieved when the kappa index and the exobase are lower.

Other ions are not considered in the present regularized model. But as explained in chapter 1, the velocity filtration explains the high temperatures of these ions observed in the corona and thus their acceleration in the solar wind with the exospheric model (Pierrard, V., Lamy, H., and Lemaire, J. (2004), Kohl et al. (2006)).

Heat flux

Figure 4.3 shows the heat flux obtained by the Maxwellian (blue), Olbertian (orange) and regularized Kappa distributions (green) divided by the heat flux obtained from the Maxwellian distribution as a function of the κ index. One observes that for low values

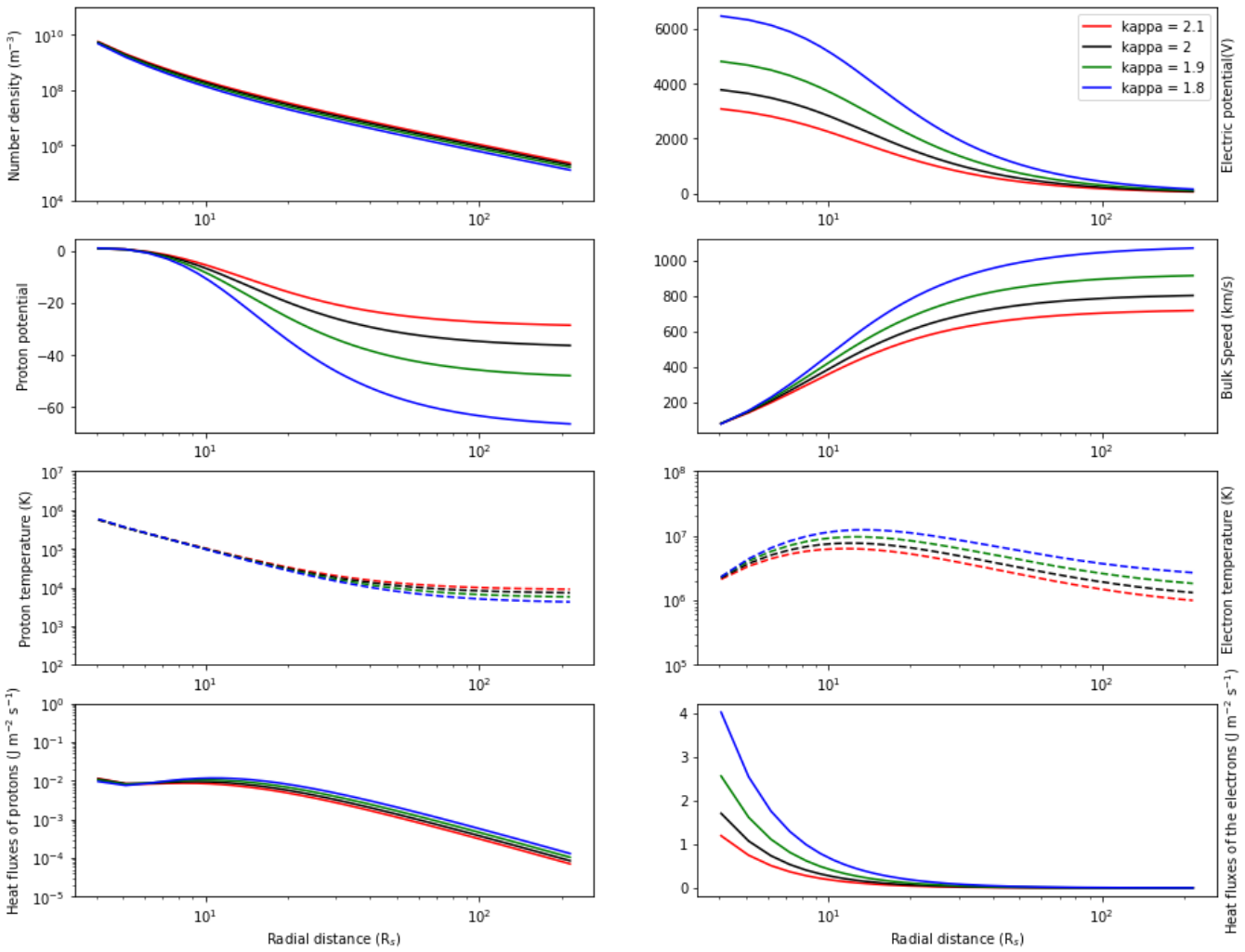

Figure 4.2: The number density, electric and proton potential, bulk speed, proton and electron temperature, heat flux of electrons and of protons calculated by the model for a κ of 1.8 (blue), 1.9 (green), 2 (black), 2.1 (red). The model took as an initial condition a proton and electron temperature of 10^6K, an exobase height of 3 R_S and goes to a radial distance of 215 R_S or 1 AU.

of the kappa index, the heat flux is very different from the Maxwellian flux contrary to the value $\kappa > 10$ where the flux is almost identical. Thus, when the suprathermal population is very large, the heat flux calculated with a Maxwellian distribution largely underestimates the latter. This non-thermal population is enhanced in fast solar wind or during energetic events. Values of κ below 10 are generally observed in the wind, but not lower than 1.

As explained in chapter 1, in the corona, the heat flux does not approach the Spitzer–Harm limit (Spitzer Härm, 1953), the expression of the heat flux in collisional plasma. This limit can only be reached when the VDF is Maxwellian ($\kappa \to \infty$). The suprathermal tails of the eVDF have a considerable impact and the classical heat conduction law cannot be applied in such a case.

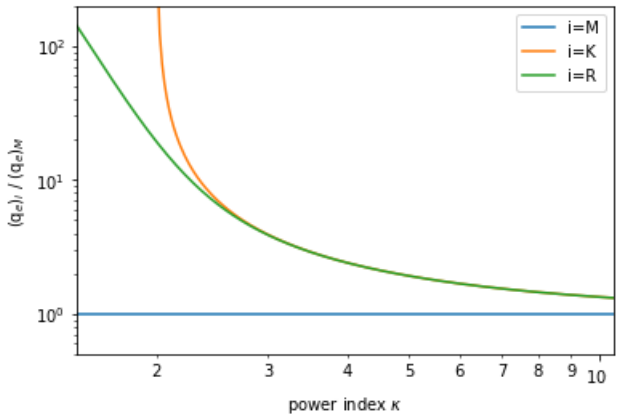

Figure 4.3: Normalized heat flux q_i/q_M of the distribution i as a function of the power index κ. The index M represents the Maxwellian distribution (blue), the index K the Olbertian distribution (orange) and the index R the regularized Kappa distribution (green).

Being more anisotropic, at low radial distances, the heat flow is mainly generated by the strahl, the antisunward beaming population parallel to the IMF. This population is enhanced in fast winds or in energetic events, like CMEs. The use of an anisotropic drifting distribution would make the results more accurate. Lazar et al. (2020b) obtained heat flux values in the case of anisotropic (and isotropic) drifting distribution with the regularized drifting bi-kappa distribution (RDBK) (see Scherer, K., Fichtner, H., and Lazar, M. (2017) for the definition).

4.3 Data

The data used for the comparison are the same as in the previous chapter. The information on time interval, distance, latitude, and sample size took for each probe can be found in table 3.1. One can thus compare the data of density, bulk speed, and proton temperature for all the satellites. The electron temperature has only been obtained by Ulysses.

4.4 Results of the comparison between the model and the observations

By looking at the radial profiles obtained in-situ from the satellites near the ecliptic, one can compare these with profiles obtained by the improved model for different kappa indices.

Figure 4.4 shows this comparison for values of κ of 3, 4, 5 and 8. The points represent the average of the data obtained at the corresponding distance and the coloured area represents the standard deviation. The colour black refers to the whole data set while the colours green and red refer to the data with a speed below and above 400 km/s

respectively. In-situ data for the other quantities calculated by the model were not provided by the different missions.

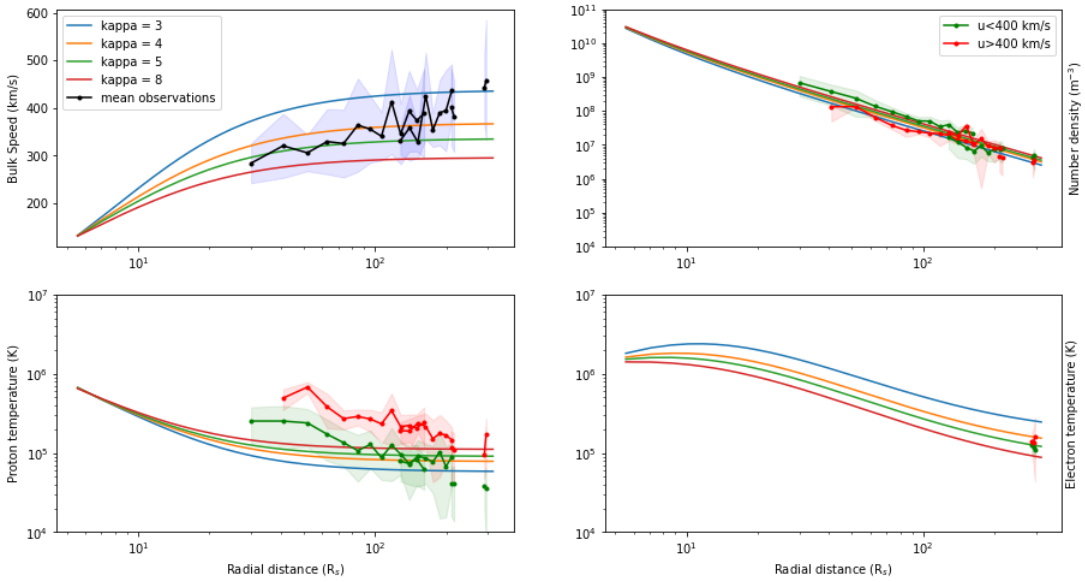

Figure 4.4: Comparison of the data of PSP, OMNI, SOLO and UY with the results of the kinetic model for a κ of 3,4,5,8. The inital parameters used in the model are an initial temperature for the proton of $1,6\ 10^6$ K, for the electron $1,4\ 10^6$ K and an altitude for the exobase of 4 R_S. The coloured area correspond to the standard deviation.

The altitude of the exobase for exospheric models is usually estimated between 2 and 10 R_S (Maksimovic et al. 1997a). However, by applying a non-monotonic proton potential, Lamy et al. (2003) showed that to correctly represent the fast winds, the exobase of coronal holes is rather between $\sim 1.1 - 5R_S$. The altitude of the exobase is related to the type of solar wind. In our model, we use the same height of the exobase for the profile with different kappa. Since we have to represent both slow and fast winds, a value of 4 R_S has been assumed. An electron temperature of 1.4 10^6K and a proton temperature of 1.6 10^6 K were chosen to represent the higher proton temperatures observed. One wants to examine which kappa value best represents the observations.

With the observed suprathermalization effect (Štverák et al. (2009)), it is expected that the eVDF shows larger suprathermal tails with distance. The bulk speed must indeed be represented by a smaller index with the distance in figure 4.4.

When comparing the density, one can infer that the radial profile of the density is well represented, by having a decrease of the form r^{-2}. The density at the exobase obtained for the distribution with a $\kappa = 3$ is 2.7 10^{10} m^{-3}. The change in the kappa index does not have much impact on the density. However, it is observed that, as the model predicts, fast winds generally have a lower density.

With the limited data, nothing can be concluded for the electron temperature profile. However, with the coronal heating problem, the temperature inversion observed with

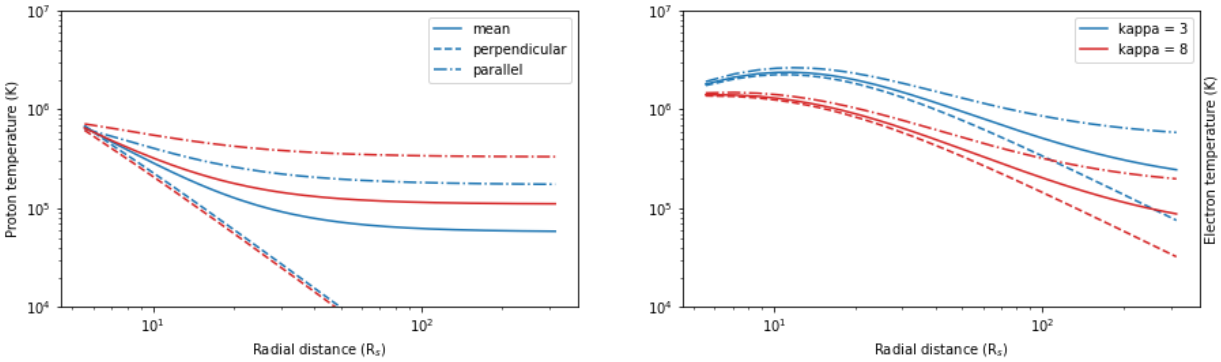

Figure 4.5: The mean, parallel and perpendicular temperatures of proton (left) and electron (right) obtained by the exospheric model for a κ of 3 and 8. The inital parameters used in the model are an initial temperature for the proton of $1,6\ 10^6$ K, for the electron $1,4\ 10^6$ K and an altitude for the exobase of 4 R_S.

these kappa values is a good indication.

The proton temperature is the only one that can be considered as poorly predicted by the model. The latter drops too fast and reaches temperature values that are too low at the closest distances from PSP. Even by changing the initial conditions of the model, one cannot obtain a profile that matches.

Figure 4.5 represents the radial profile of the perpendicular, parallel and mean temperature of the protons and electrons for the $\kappa = 3, 8$ with the same initial conditions. It is observed that the temperature anisotropy increases very strongly with the radial distance and is not consistent with observations.

The temperature anisotropy of electron and proton is probably poorly defined because the model does not consider interactions and conserves the magnetic moment. Pierrard et al. (2001) showed that adding a spiral magnetic field reduced the anisotropy of the proton. However, the observations were still not consistent with the proton temperature anisotropy. To obtain a valid profile, and further reduce the excessive proton anisotropy, one must therefore consider the Coulomb collisions and wave-particle interactions like in Pierrard, V., Maksimovic, M., and Lemaire, J. (2001) for Coulomb collisions and Pierrard, V., Lazar, M., and Schlickeiser, R. (2011) for whistler waves. These two interactions act on the isotropy by pitch angle scattering on the distributions but do not fundamentally modify the average of the parameters obtained. The average temperature remains unchanged. With the spiral field, the total electron temperature was increased, and the total proton temperature decreased (Pierrard et al. (2001)).

As discussed in Chapter 3, there is a link in the observations between the proton temperature and the solar wind bulk speed. The latter does not appear in the exospheric model. Indeed, a slow wind with a high kappa index is associated with a higher temperature profile. One can thus understand that this link is, at least in part, due to Coulomb collisions and wave-particle interactions that are not included in the model.

By neglecting these interactions, the model does not correctly reproduce the temperature.

4.5 Discussion

The use of the RKD allows a more realistic representation of macroscopic thermodynamic quantities. By being able to compute them for all kappas, a fluid description that considers suprathermal particles is now achievable. To have a more realistic model, a combination of the kinetic and a fluid model that considers the magnetic field (magnetohydrodynamics (MHD) model) would be beneficial.

This simple exospheric model gave a good insight into what happens when the interactions are neglected. The velocity filtration effect allows explaining the acceleration of the winds and the coronal heating problem without having to involve an additional source of energy or waves. Also, the model represents relatively well the moments like density and velocity, but the temperature anisotropy and the heat flux are too large

As mentioned in the previous chapter, temperature anisotropy helps to identify the mechanisms that shape the solar wind. The addition of the spiral magnetic field is not sufficient to solve this problem. Wilson III et al. (2018) showed that wave-particle interactions rate were of the same order or even higher than the Coulomb interaction rates at 1 AU. Therefore, wave-particle interactions cannot be neglected in the modelling of solar wind.

Coulomb collisions affect weakly the suprathermal particles. However, models that have incorporated Coulomb interactions in the corona and at low altitudes, such as the model of Pierrard et al. (2001c), have shown that in kinetic models, Coulomb collisions reduce the large temperature anisotropy. The Coulomb interactions mainly modify the scattering of the pitch angle and keep the average of the moments stable. Nevertheless, it explains with difficulty the halo of the particles, the anisotropy of the core and the strahl population parallel to the IMF. Other interactions must therefore be considered.

The pitch angle scattering of the strahl in the halo is considered to be the result of wave-particle interactions, caused by kinetic instability (Vocks et al. (2005), Maksimovic et al. (2005), Štverák et al. (2009)). Waves such as Alfven waves can also dissipate energy. These waves can form a proton beam and make the core of ions anisotropic Pierrard, V. and Voitenko, Y. (2013).

The heat flux has a major role in the model. Thus, the determination of the latter must be the most accurate possible. The suprathermal populations of the eVDF, generating the heat flux, can be considered as the instability of the heat flux. As mentioned in chapter 2, the halo can deviate from the isotropy and generate a firehose instability ($A_h < 1$) or an electron-cyclotron instability (also named whistler) ($A_h > 1$). The study of their distribution is more relevant with a κ-dependent temperature to represent properly the effect of the instability through the kappa parameter (Lazar et al. (2017a)).

By studying the radial evolution of heat flux instabilities, Sun, H. et al. (2021) showed how several heat flux instabilities could impact the anisotropy and the distribution.

The electron distribution typically has temperature anisotropy and beam. Since the heating process is the velocity filtration, one can easily understand that the lack of these interactions in the model will generate excessive anisotropies and heat flow.

The low altitude boundary conditions in the model allow for better results. Future PSP data at even lower distances will provide additional insights to improve the model.

Chapter 5

Conclusion

As shown in this master thesis, the Kappa distribution is very useful for modelling solar winds. This distribution allows to represent well the power laws that can generally be found in space plasmas. When one refers to the Kappa distribution, one really designates a whole family of distributions. The choice of the distribution depends on characteristics such as isotropy, drift,... as well as on the physical interpretation. The most interesting distributions recently introduced is the regularized Kappa distribution. The latter allows to remove critical limitations present in the other distributions but also has a physical motivation as it does not consider superluminal particles.

The main objective of this master was the improvement of an exospheric model with the regularized distribution allowing the calculation of moments for kappas lower than 2. A comparison with data from several satellites was performed to determine the validity of the model. The Parker Solar Probe data allowed to compare the model results with in-situ data at small distances but also to analyze the characteristics of the VDF at a distance of 17.2 R_S. The model calculates the moments thanks to a VDF given for the exobase. Thus, the analysis also allows to determine if this chosen distribution is realistic. Finally, an analysis of the parameters of the solar wind has been made to identify some phenomena taking place in its evolution. These parameters have been confronted with the results of the exospheric model.

First, I have fitted velocity distribution functions of electrons and protons observed by PSP at 17.2 R_S, and this demonstrated that suprathermal particles are well present also at this low distance from the Sun. Two power laws were observed. The global Olbertian distribution, used in the model, by itself was able to represent relatively well all energies. For some angles, this distribution could have kappa close to 2 and by succeeding in modelling the superhalo, could have not considered the cutoff necessary for speeds approaching the speed of light, leading to the divergence of some moments. This motivates the choice of a regularized distribution that I have implemented in the model. To represent more accurately the eVDF up to high energies, the distribution must therefore be determined by 4 populations: the core, halo, strahl and superhalo. In the studied distribution, only the strahl direction needed to be represented by a small kappa. The presence of a superhalo, at energies just below the relativistic energy range, shows the importance of using distributions that neglect non-realistic velocities ($v > c$).

The study of the links between the parameters shows that relations can be found between the different populations. The observed pitch angle scattering phenomenon seems to be explained by wave-particle interactions. Indeed, the deviation from isotropy can induce instabilities that will have the effect of generating waves to reduce the deviation. With the interactions between the different populations, it is useful to study the evolution of the populations in a collective way to understand the mechanisms. Concerning the protons, the not completely understood link between velocity and temperature has been observed even at small distances. It is the first time that velocity distribution functions of particles and their moments are observed so close to the Sun.

By comparing the model with in-situ data at different distances during a minimum of solar activity, one can observe that a kappa lower than 2 is not necessary to represent the solar winds. However, this change is interesting from a fundamental point of view and this model can be used to describe other plasma escaping from other stars or planetary bodies. The model represents the densities and velocities relatively well but the temperature anisotropy and the heat flux are too large. The addition of a spiral magnetic field helps to decrease the anisotropy but it is still excessive. As can be understood from the links between the parameters and from the existence of heat flux instabilities, interactions must be added.

The origins of the suprathermal populations can be explained by different mechanisms and are still discussed. The halo has several explanations for its presence including the scattering of electrons from the strahl into the halo. Being present during a quiet solar activity, the superhalo is probably due to a wave-particle interaction. To study these interactions, the Olbertian distribution with a κ-dependent temperature is more relevant. The model, using the velocity filtration process, does not provide an answer to the question of the origin of suprathermal particles. It explains the acceleration and heating of the solar wind but implies a truncated VDF at high altitudes. Indeed, the suprathermal population in the parallel direction and towards the Sun cannot escape. Therefore, the exospheric model cannot explain the evolution of the shape of the VDF. It is the interactions that have this role. An increase in collisions would imply a distribution tending more to a Maxwellian. Thus, the particle-particle interactions act mainly on the thermal particles and the wave-particle interactions on the suprathermal particles.

Finally, since in-situ data at lower altitudes become accessible over time, the radial evolution of solar wind particles will be better understood. These observations may allow a more accurate determination of the initial conditions and to impose boundary conditions on the model. Also, if in the future electron data become available, a comparison with the electron temperature may be possible. Furthermore, now that the regularized Kappa allows a modelization for all kappas, a combination with a fluid model would allow a better understanding of the phenomena acting on the solar wind.

Bibliography

Anderson, B. R. et al. (2012). "Variability of the solar wind suprathermal electron strahl". In: *Journal of Geophysical Research: Space Physics* 117.A4. DOI: 10.1029/2011JA017269.

Arya, S. and Freeman, J. W. (1991). "Estimates of solar wind velocity gradients between 0.3 and 1 AU based on velocity probability distributions from Helios 1 at perihelion and aphelion". In: *Journal of Geophysical Research: Space Physics* 96.A8, pp. 14183–14187.

Berčič, L. et al. (2020). "Coronal Electron Temperature Inferred from the Strahl Electrons in the Inner Heliosphere: Parker Solar Probe and Helios Observations". In: *The Astrophysical Journal* 892.2, p. 88. DOI: 10.3847/1538-4357/ab7b7a.

Binsack, J. (1966). "Plasma studies with the IMP-2 satellite." PhD thesis. Massachusetts Institute of Technology.

Burlaga, L.F. and Ogilvie, K.W. (1970). "Magnetic and thermal pressures in the solar wind". In: *Solar Physics* 15.1, pp. 61–71.

Cranmer, S. R. (2002). "Coronal holes and the high-speed solar wind". In: *Space Science Reviews* 101.3, pp. 229–294.

Elliott, H. A. et al. (2012). "Temporal and radial variation of the solar wind temperature-speed relationship". In: *Journal of Geophysical Research: Space Physics* 117.A9. DOI: 10.1029/2011JA017125.

Elliott, H.A., McComas, D. J., and DeForest, C.E. (2016). "Long–term trends in the solar wind proton measurments". In: *The Astrophysical Journal* 832.1, p. 66. DOI: 10.3847/0004-637x/832/1/66.

Fichtner, H. and M. Lazar (2021). "Introduction and Motivation". In: *Kappa Distributions*. Springer, pp. 3–12.

Fichtner, H. et al. (2018). "Entropy of plasmas described with regularized κ distributions". In: *Physical Review E* 98.5, p. 053205. DOI: 10.1103/PhysRevE.98.053205.

Gosling, JT. et al. (1987). "Bidirectional solar wind electron heat flux events". In: *Journal of Geophysical Research: Space Physics* 92.A8, pp. 8519–8535.

Halekas, J. S. et al. (2020). "Electrons in the Young Solar Wind: First Results from the Parker Solar Probe". In: *The Astrophysical Journal Supplement Series* 246.2, p. 22. DOI: 10.3847/1538-4365/ab4cec.

Jockers, K. (1970). "Solar wind models based on exospheric theory". In: *Astronomy and Astrophysics* 6, p. 219.

Kasper, J.C. et al. (2016). "Solar wind electrons alphas and protons (SWEAP) investigation: Design of the solar wind and coronal plasma instrument suite for solar probe plus". In: *Space Science Reviews* 204.1, pp. 131–186. DOI: 10.1007/s11214-015-0206-3.

Kim, S. et al. (2016). "Suprathermal solar wind electrons and langmuir turbulence". In: *The Astrophysical Journal* 828.1, p. 60. DOI: 10.3847/0004-637x/828/1/60.

Kohl, J. L. et al. (2006). "Ultraviolet spectroscopy of the extended solar corona". In: *The Astronomy and Astrophysics Review* 13.1, pp. 31–157. DOI: 10.1007/s00159-005-0026-7.

Lamy, H. et al. (2003). "A kinetic exospheric model of the solar wind with a nonmonotonic potential energy for the protons". en. In: *Journal of Geophysical Research: Space Physics* 108.A1. ISSN: 2156-2202. DOI: 10.1029/2002JA009487.

Landi, S., Matteini, L., and Pantellini, F. (2014). "Electron heat flux in the solar wind: Are we observing the collisional limit in the 1 AU data?" In: *The Astrophysical Journal Letters* 790.1, p. L12. DOI: 10.1088/2041-8205/790/1/L12.

Landi, S. and Pantellini, F.G.E. (2001). "On the temperature profile and heat flux in the solar corona: Kinetic simulations". In: *Astronomy & Astrophysics* 372.2, pp. 686–701.

Lazar, M. et al. (2017a). "Dual Maxwellian-Kappa modeling of the solar wind electrons: new clues on the temperature of Kappa populations". In: *Astron. Astrophys* 602, A44. DOI: 10.1051/0004-6361/201630194.

Lazar, M. et al. (2017b). "Dual Maxwellian-Kappa modeling of the solar wind electrons: new clues on the temperature of Kappa populations". In: *Astronomy & Astrophysics* 602, A44. DOI: 10.1051/0004-6361/201630194.

Lazar, M. et al. (2020a). "Characteristics of solar wind suprathermal halo electrons". en. In: *Astronomy & Astrophysics* 642. Publisher: EDP Sciences, A130. ISSN: 0004-6361, 1432-0746. DOI: 10.1051/0004-6361/202038830.

Lazar, M. et al. (2020b). "Toward a realistic macroscopic parametrization of space plasmas with regularized -distributions". en. In: *Astronomy & Astrophysics* 634. Publisher: EDP Sciences, A20. ISSN: 0004-6361, 1432-0746. DOI: 10.1051/0004-6361/201936861.

Lazar, M., Fichtner, H., and Yoon, P.H. (2016). "On the interpretation and applicability of κ-distributions". In: *Astronomy & Astrophysics* 589, A39. DOI: 10.1051/0004-6361/201527593.

Le Chat, G. et al. (2011). "Large-scale variation of solar wind electron properties from quasi-thermal noise spectroscopy: Ulysses measurements". In: *Solar Physics* 271.1, pp. 141–148. DOI: 10.1007/s11207-011-9797-3.

Lemaire, J. and Scherer, M. (1971). "Kinetic models of the solar wind". In: *Journal of Geophysical Research* 76.31, pp. 7479–7490.

Lin, R. P. (1998). "Wind Observations of Suprathermal Electrons in the Interplanetary Medium". In: *The Advanced Composition Explorer Mission*. Ed. by C. T. Russell, R. A. Mewaldt, and T. T. Von Rosenvinge. Dordrecht: Springer Netherlands, pp. 61–78. ISBN: 978-94-011-4762-0. DOI: 10.1007/978-94-011-4762-0_4.

Maksimovic, M. et al. (2005). "Radial evolution of the electron distribution functions in the fast solar wind between 0.3 and 1.5 AU". In: *Journal of Geophysical Research: Space Physics* 110.A9. DOI: 10.1029/2005JA011119.

Maksimovic, M. et al. (2020). "Anticorrelation between the Bulk Speed and the Electron Temperature in the Pristine Solar Wind: First Results from the iParker Solar Probe/i and Comparison with iHelios/i". In: *The Astrophysical Journal Supplement Series* 246.2, p. 62. DOI: 10.3847/1538-4365/ab61fc.

Maksimovic, M., Pierrard, V., and Lemaire, J.F. (1997). "A kinetic model of the solar wind with Kappa distribution functions in the corona." In: *Astronomy and Astrophysics* 324, pp. 725–734.

Maksimovic, M., Pierrard, V., and Riley, P. (1997). "Ulysses electron distributions fitted with Kappa functions". In: *Geophys. Res. Let.* 24.9, pp. 1151–1154. DOI: 10.1029/97GL00992.

Marsch, E. et al. (1982). "Solar wind protons: Three-dimensional velocity distributions and derived plasma parameters measured between 0.3 and 1 AU". In: *Journal of Geophysical Research: Space Physics* 87.A1, pp. 52–72.

Matthaeus, W. H., Elliott, H. A., and McComas, D. J. (2006). "Correlation of speed and temperature in the solar wind". In: *Journal of Geophysical Research: Space Physics* 111.A10. DOI: 10.1029/2006JA011636.

Melkumyan, A. A. et al. (2020). "Behavior of the speed and temperature of the solar wind during interplanetary disturbances creating Forbush decreases". In: *Geomagnetism and Aeronomy* 60.5, pp. 521–529. DOI: 10.1134/S0016793220040106.

Moncuquet, M. et al. (2020). "First In Situ Measurements of Electron Density and Temperature from Quasi-thermal Noise Spectroscopy with iParker Solar Probe/i/FIELDS". In: *The Astrophysical Journal Supplement Series* 246.2, p. 44. DOI: 10.3847/1538-4365/ab5a84.

Pierrard, V. (2012a). "Kinetic Models of Solar Wind Electrons, Protons and Heavy Ions". In: *Exploring the Solar Wind*. Ed. by Marian Lazar. Rijeka: IntechOpen. Chap. 10. DOI: 10.5772/39278.

— (2012b). "Solar wind electron transport: interplanetary electric field and heat conduction". In: *Space science reviews* 172.1, pp. 315–324. DOI: 10.1007/s11214-011-9743-6.

Pierrard, V. et al. (2001). "Collisionless model of the solar wind in a spiral magnetic field". In: *Geophysical research letters* 28.2, pp. 223–226. DOI: 10.1029/2000GL011888.

Pierrard, V. et al. (2016). "The Electron Temperature and Anisotropy in the Solar Wind. Comparison of the Core and Halo Populations". en. In: *Solar Physics* 291.7, pp. 2165–2179. ISSN: 1573-093X. DOI: 10.1007/s11207-016-0961-7.

Pierrard, V. and Lamy, H. (2003). "The effects of the velocity filtration mechanism on the minor ions of the corona". In: *Solar Physics* 216.1, pp. 47–58. DOI: 10.1023/A:1026157306754.

Pierrard, V., Lamy, H., and Lemaire, J. (2004). "Exospheric distributions of minor ions in the solar wind". In: *Journal of Geophysical Research: Space Physics* 109.A2. DOI: 10.1029/2003JA010069.

Pierrard, V. and Lazar, M. (2010). "Kappa distributions: theory and applications in space plasmas". In: *Solar Physics* 267.1, pp. 153–174. DOI: 10.1007/s11207-010-9640-2.

Pierrard, V., Lazar, M., and Schlickeiser, R. (2011). "Evolution of the electron distribution function in the whistler wave turbulence of the solar wind". In: *Solar Physics* 269.2, pp. 421–438. DOI: 10.1007/s11207-010-9700-7.

Pierrard, V., Lazar, M., and Štverák, S. (2020). "Solar Wind Plasma Particles Organized by the Flow Speed". en. In: *Solar Physics* 295.11, p. 151. ISSN: 1573-093X. DOI: 10.1007/s11207-020-01730-z.

Pierrard, V. and Lemaire, J. (1996). "Lorentzian ion exosphere model". en. In: *Journal of Geophysical Research: Space Physics* 101.A4, pp. 7923–7934. ISSN: 2156-2202. DOI: 10.1029/95JA03802.

Pierrard, V., Maksimovic, M., and Lemaire, J. (2001). "Self-consistent model of solar wind electrons". In: *Journal of Geophysical Research: Space Physics* 106.A12, pp. 29305–29312. DOI: 10.1029/2001JA900133.

Pierrard, V. and Voitenko, Y. (2013). "Modification of proton velocity distributions by Alfvénic turbulence in the solar wind". In: *Solar Physics* 288.1, pp. 355–368. DOI: 10.1007/s11207-013-0294-8.

Rosenbauer, H. et al. (1977). "A survey on initial results of the Helios plasma experiment". In: *Journal of Geophysics Zeitschrift Geophysik* 42.6, pp. 561–580.

Scherer, K. et al. (2019a). "Moments of the Anisotropic Regularized κ-distributions". en. In: *The Astrophysical Journal* 880.2. Publisher: American Astronomical Society, p. 118. ISSN: 0004-637X. DOI: 10.3847/1538-4357/ab1ea1.

Scherer, K. et al. (2019b). "On the Applicability ofκ-distributions". In: *The Astrophysical Journal* 881.2, p. 93. DOI: 10.3847/1538-4357/ab2df9.

Scherer, K., Fichtner, H., and Lazar, M. (2017). "Regularized κ-distributions with non-diverging moments". In: *EPL (Europhysics Letters)* 120.5, p. 50002. DOI: 10.1209/0295-5075/120/50002.

Scudder, J. D. (1992a). "On the causes of temperature change in inhomogeneous low-density astrophysical plasmas". In: *The Astrophysical Journal* 398, pp. 299–318.

Scudder, J. D. (1992b). “Why all stars should possess circumstellar temperature inversions”. In: *The Astrophysical Journal* 398, pp. 319–349.

Shoub, E. C. (1983). “Invalidity of local thermodynamic equilibrium for electrons in the solar transition region. I - Fokker-Planck results”. In: 266, pp. 339–369. DOI: 10.1086/160783.

Štverák, Š. et al. (2008). “Electron temperature anisotropy constraints in the solar wind”. In: *Journal of Geophysical Research: Space Physics* 113.A3. DOI: 10.1029/2007JA012733.

Štverák, S. et al. (2009). “Radial evolution of nonthermal electron populations in the low-latitude solar wind: Helios, Cluster, and Ulysses Observations”. In: *Journal of Geophysical Research* 114. DOI: 10.1029/2008JA013883.

Sun, H. et al. (2021). “Electron Heat Flux Instabilities in the Inner Heliosphere: Radial Distribution and Implication on the Evolution of the Electron Velocity Distribution Function”. In: *The Astrophysical Journal Letters* 916.1, p. L4. DOI: 10.3847/2041-8213/ac0f02.

Vasyliunas, V. M. (1968). “A survey of low-energy electrons in the evening sector of the magnetosphere with OGO 1 and OGO 3”. In: *Journal of Geophysical Research* 73.9, pp. 2839–2884.

Verscharen, D., Klein, K. G., and Maruca, B. A. (2019). “The multi-scale nature of the solar wind”. In: *Living Rev Sol Phys* 16.1. DOI: 10.1007/s41116-019-0021-0.

Vocks, C. et al. (2005). “Electron halo and strahl formation in the solar wind by resonant interaction with whistler waves”. In: *The Astrophysical Journal* 627.1, p. 540. DOI: 10.1086/430119.

Wang, L. et al. (2012). “Quiet-time interplanetary 2–20 keV superhalo electrons at solar minimum”. In: *The Astrophysical Journal Letters* 753.1, p. L23. DOI: 10.1088/2041-8205/753/1/L23.

Wang, L. et al. (2015). “Solar wind 20–200 keV superhalo electrons at quiet times”. In: *The Astrophysical Journal Letters* 803.1, p. L2. DOI: 10.1088/2041-8205/803/1/L2.

Watari, S. (2018). “Intense geomagnetic storms associated with coronal holes under the weak solar-wind conditions of cycle 24”. In: *Solar Physics* 293.2, pp. 1–12. DOI: 10.1007/s11207-018-1248-y.

Whittlesey, P. L. et al. (2020). “The Solar Probe ANalyzers—electrons on the parker solar probe”. In: *The Astrophysical Journal Supplement Series* 246.2, p. 74. DOI: 10.3847/1538-4365/ab7370.

Wilson III, L. et al. (2018). “The Statistical Properties of Solar Wind Temperature Parameters Near 1 au”. In: *The Astrophysical Journal Supplement Series* 236.2, p. 41. DOI: 10.3847/1538-4365/aab71c.

Yang, L. et al. (2015). "The angular distribution of solar wind superhalo electrons at quiet times". In: *The Astrophysical Journal* 811.1, p. L8. DOI: 10.1088/2041-8205/811/1/l8.

Zouganelis, I. et al. (2005). "Acceleration of weakly collisional solar-type winds". In: *The Astrophysical Journal* 626.2, p. L117. DOI: 10.1086/431904.

UNIVERSITE CATHOLIQUE DE LOUVAIN

Faculté des sciences

Place des sciences, 2 bte L6.06.01, 1348 Louvain-la-Neuve, Belgique | **www.uclouvain.be/sc**